

Mechanisms of interlayer exciton emission and giant valley polarization in van der Waals heterostructures

Eronildo C. Castro ¹, David S. Brandão ¹, Helena Bragança ^{1,2}, A. S. Martins,³ Flavio Riche,⁴
A. C. Dias ^{1,2}, J. H. Zhao,⁵ A. L. A. Fonseca ^{1,2} and Fanyao Qu ^{1,2,*}

¹*Instituto de Física, Universidade de Brasília, Brasília-DF 70919-970, Brazil*

²*International Center for Condensed Matter Physics, University of Brasília, P.O. Box 04513, Brasília 70910-900, Brazil*

³*Departamento de Física - ICEx, Universidade Federal Fluminense, Volta Redonda-RJ 27213-145, Brazil*

⁴*CeFEMA, Instituto Superior Técnico, Universidade de Lisboa, Av. Rovisco Pais, 1049-001 Lisbon, Portugal*

⁵*Department of Physics, Jining University, Qufu 273155, China*



(Received 18 August 2022; revised 4 December 2022; accepted 13 January 2023; published 30 January 2023)

We perform a theoretical investigation about the valley dynamics of interlayer excitons (IXs) in MoS₂/WS₂ heterostructure with AB stacking configuration grown on ferromagnetic substrate. We find that the interlayer charge transfer process changes dramatically the IX emission as well as its valley polarization (VP). The magnetic proximity effect (MPE) exerted by ferromagnetic substrate, on the other hand, generates a zero-field valley Zeeman splitting, which suppresses the depolarization induced by electron-hole exchange interaction. Remarkably, unlike usual exciton-phonon scattering, which is harmful to the VP, the phonon-assisted intervalley scatterings between two split IX states in the different valleys foster an IX population imbalance in these states, giving rise to a giant VP. A combination of these experimentally tunable physical quantities (interlayer charge transfer rate, MPE intensity and exciton-phonon coupling strength) provides a promising tool for intriguing emerging magneto-optical emissions and their VPs. Considering a large family of layered materials, this study sheds light on the path for development of van der Waals heterostructures with detectable IX emissions and giant VP.

DOI: [10.1103/PhysRevB.107.035439](https://doi.org/10.1103/PhysRevB.107.035439)

I. INTRODUCTION

Monolayer (ML) transition metal dichalcogenides (TMDs) feature strong Coulomb interactions [1–3] due to the two-dimensional (2D) spatial confinement and the reduced dielectric screening. Light excitation leads to the formation of tightly bound electron-hole pairs named direct (intralayer) excitons (DX) [4]. Because of their high binding energies—up to a few hundred meV—they are stable even at room temperature [5,6]. In addition, the lattice inversion asymmetry of the ML TMDs along with strong spin-orbit coupling (SOC) leads to the joint of spin and valley degrees of freedom and valley optical selection rules, which holds promising applications in novel valleytronic devices [7]. However, the large oscillator strength and strong electron-hole Coulomb interaction limit both their radiative- and valley-lifetimes [8,9], undermining their potential for applications.

The 2D materials, such as ML TMDs, can form van der Waals (vdWs) heterostructures held together by weak van der Waals forces, providing an unprecedented platform to engineer quantum materials with exotic physical properties [10]. Among the different vdWs heterostructures, the most interesting ones for applications are those characterized by a type II band alignment where the valence band (VB) maximum and the conduction band (CB) minimum lie in different lay-

ers. This configuration energetically promotes ultrafast charge separation, yielding the photoexcited electrons to reside on one TMD layer and for the holes to be on the other. Interestingly, these vdW heterostructures not only inherit the valley contrasting properties from the constituent TMD layers, but also often exhibit novel features and functionalities. For instance, the rotational misalignment or lattice mismatch in the semiconducting TMD heterostructures leads to the formation of moiré potentials. Recently, Moiré potential trapped excitons, called moiré excitons, have been experimentally observed, which provides an analog to ultracold atoms in optical lattices or photons in photonic crystals [11–17].

The spatial separation between the electrons and holes leads to the formation of indirect interlayer excitons (IXs) in vdW heterostructures, see Fig. 1(a) for a schematic representation of DX and IX in MoS₂/WS₂ heterostructures. Experimentally, the presence of an IX is featured by the emergence of an extra photoluminescence (PL) peak at a lower energy along with quenching of the PL of the DX in the constituent MLs [18]. In addition, the reduced spatial overlap of the electron—hole wave functions weakens dramatically electron—hole Coulomb interaction. Therefore, the IXs are characterized by recombination times several orders of magnitude longer than the DXs and a long-lived valley polarization (VP). These properties make IXs ideally suited for valleytronic applications [7,11–17,19,20].

The recent discoveries of 2D ferromagnets [21,22] bring the possibility of 2D ferromagnetic vdW heterostructures [23] such as the TMD ML grown on ferromagnetic substrate. The

*Deceased.

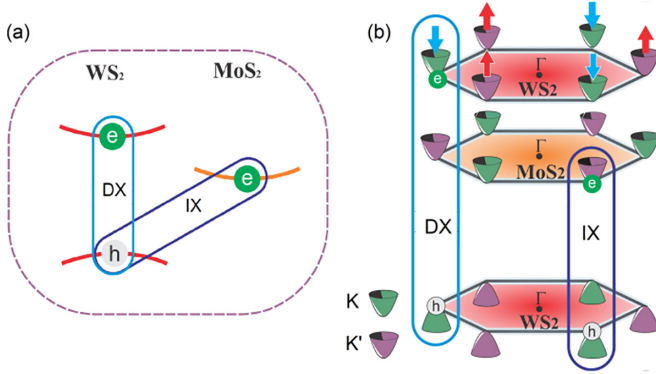


FIG. 1. Schematic representation of (a) the relevant band edges of MoS_2/WS_2 vdWs heterostructures with AB stacking, formation of DX in WS_2 layer and IX with the electron located in the CB of MoS_2 and the hole in the VB of WS_2 , and (b) the first Brillouin zone. The arrows indicate the spin states. The α valley of the heterostructure is formed by the K valley of WS_2 and the K' valley of MoS_2 , while β valley comprises the K' valley of WS_2 and the K valley of MoS_2 .

TMD ML itself is a nonmagnetic semiconductor with valley contrast property, but without valley Zeeman splitting (VS). By interfacing it with a ferromagnetic insulator, however, the proximity-induced exchange field gives rise to spontaneous VS. Therefore, the magnetic proximity effect (MPE) exerted by ferromagnetic substrate may enable the valley-specific band engineering and application of these materials in novel magneto-optical and valleytronic devices. Although an external magnetic field applied perpendicular to the TMD plane can also produce a Zeeman splitting, very high fields [24] would be required to produce the same order of VS achieved by MPE. Recently, the manipulation of the valley degree of freedom via MPE has been successfully demonstrated for the DXs in TMD MLs [25,26]. Since the effective g factor of IXs is much bigger than that of the DXs [10], the impact of MPE on optical properties of the vdWs heterostructures is much more pronounced, leading to experimental observations of a giant VS and a subsequent near-unity VP [27].

As aforementioned, the IXs possess the recombination times and valley lifetimes several orders of magnitude longer than the DXs, making them ideally suited for some spintronics and valleytronic device applications. However, a weak interlayer vdW interaction inhibits interlayer charge transfer across vdW heterostructures, which significantly constrains the population of the IXs, and the reduced oscillator strength of IXs renders them further darkish. The small population together with the darkness of the IXs substantially limit their experimental probing and potential applications.

Extensive studies on pristine vdWs TMD heterostructures, including electronic band structures as well as optical properties, have been performed both theoretically and experimentally [7,15,19]. Recently, magneto-PL measurements showing that an out-of-plane magnetic field magnitude required for an intermediate VS is as high as a few ten Teslas have been reported [10,28,29]. This high magnetic field makes practical applications difficult. Therefore, although the IXs host many fascinating physical properties such as giant effective g factor, long radiative relaxation and valley lifetimes, the following challenges are still facing for the real

applications: Darkness of the IXs and high magnetic field required to achieve a large VS. To overcome these challenges, a deep understanding of IX dynamics in vdWs materials such as MoS_2/WS_2 heterostructure is crucial. Figure 1 shows a schematic representation of DX and IX excitons in AB stacking: the K (K') valley of WS_2 and the K' (K) valley of MoS_2 are aligned, forming the α (β) valley. In this paper, we have developed the first principles, low-energy $\mathbf{k} \cdot \mathbf{p}$ model considering also exciton quasiparticles, plus coupled rate equation calculations for studying IX dynamics in MoS_2/WS_2 vdW heterostructure with AB stacking configuration grown on ferromagnetic substrate. The dependence of IX emissions and VP on the interlayer charge transfer rate, exciton-phonon interaction strength, MPE as well as the helicity of excitation light beams has been explored. We find that the MPE can generate a giant zero-field VS. In addition, unlike usual exciton-phonon coupling induced intervalley scatterings, which are harmful to the VP, the phonon-assisted intervalley scatterings between two splitting IX states in two opposite valleys foster an imbalance of IX populations in these states, giving rise to an enhanced VP. Tuning exciton-phonon coupling strength can dramatically modify the emerging magneto-optical behavior. For the vdWs heterostructures with large exciton-phonon coupling strength, the unity VP can be achieved even at very small MPE. Our results might be used as a guide to fabricate the vdW heterostructures with detectable IX emission and giant VP.

The paper is organized as follows: In Sec. II we describe our theoretical framework, including DFT calculations, which give rise to a complete electronic band structure and the low-energy effective model that captures the essential low-energy physics of MoS_2/WS_2 vdWs heterostructures with AB stacking and magnetic vdWs heterostructures. We also present Berry curvature and valley magnetic moment calculations. Furthermore, we report our theory about valley dynamics of interlayer excitons. In Sec. III we discuss the most relevant qualitative features of the solutions obtained, finishing with Sec. IV where we give a brief account of the results obtained.

II. THEORETICAL FRAMEWORK

To investigate optical properties of the TMD vdWs heterostructures, we build on a comprehensive theoretical framework. It is constituted by the following steps: First, we perform first-principles calculations based on density functional theory (DFT) to get the complete band structure of MoS_2/WS_2 heterostructure. Since the relevant physics of the excitonic quasiparticles is mainly determined by the low energy bands nearby the K and K' points, we employ an effective massive Dirac fermion model ($\mathbf{k} \cdot \mathbf{p}$ model) in the following calculations. The parameters involving in this approach are determined by fitting of the band structure obtained from the $\mathbf{k} \cdot \mathbf{p}$ model to the DFT-band structure. After that, we incorporate MPE in the Hamiltonian of $\mathbf{k} \cdot \mathbf{p}$ model. Diagonalizing the Hamiltonian matrix, we obtain single-particle energies and wave functions. We also consider corrections due to the exciton binding energies and calculate the lifetimes, which serve as input parameters for studying the exciton dynamics. The whole theoretical framework is presented systematically in the following subsections.

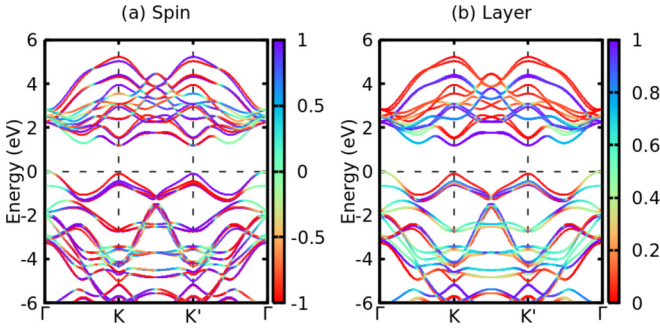


FIG. 2. (a) Spin and (b) layer resolved band structure of MoS₂/WS₂ heterostructure. The color bar in (a) indicates the spin state, while it displays the layer information in (b).

A. First principles calculations

To reveal the features of band structure and charge transfer between two TMD layers, we start by using DFT first principles calculations, employing the Vienna *ab initio* simulation package (VASP) [30,31] with the generalized gradient approximation of Perdew-Burke-Ernzerhof functional [32]. Furthermore, the projected-augmented wave approach for electron and ion interaction were used. The interlayer van der Waals interactions were described by the van der Waals density functional method of version 2 (vdW-DF2) [33]. A 600-eV energy cutoff was used for geometry optimization and electronic structure calculations and a convergence criteria of 10^{-6} eV for the self-consistent calculation was adopted. Geometry optimization for both lattice constants and atomic coordinates with $11 \times 11 \times 1$ Γ -centered Monkhorst-Pack mesh was carried out until residual forces on each atom were smaller than 0.005 eV/Å. A six-atom bilayer heterostructure consisting of MoS₂/WS₂ unit cells were built in which a 30-Å vacuum depth along the z axis to eliminate spurious interactions between the systems from their images. The lattice parameters of MoS₂ and WS₂ single-layers are almost commensurate, justifying the construction of the heterostructure of AB stacking [34–36]. The optimized lattice constants were 3.182 Å in x and y directions. To correctly account for the strong spin-orbit coupling arising from heavy atoms in TMDs, Mo and W [25,37], the spin-orbit coupling corrections were included in the electronic property calculations. The valence electron configurations include Mo $4p^6 4d^5 5s^1$ electrons, W $5d^4 6s^2$ electrons, and S $3s^2 3p^4$ electrons.

Because the α (β) valley of the heterostructure is concordant with the K (K') valley of WS₂ ML, sometimes, we use K (K') valley of WS₂ ML to refer to α (β) valley of MoS₂/WS₂. The band structure of the MoS₂/WS₂ heterostructure obtained by DFT calculation is shown in Fig. 2 in which the color code indicates (a) spin and (b) layer mean values of each

band. Our DFT results show that the valence band maximum is at Γ point, consistently with other results reported in the literature [38]. However, the energy difference between the Γ and K points is very small. Furthermore, the highest point of the valence band can be modulated by the interlayer distance. Therefore, similar to TMD MLs, the most optical processes might still occur at K points. In addition, we observe that the CBM calculated at either K or K' point is localized at MoS₂ layer, while the VBMs are hybridized states, which are delocalized among the two layers, although the weight of WS₂ ML is much larger than that of MoS₂ ML [see the colors of the curves in panel (b)].

B. Effective massive Dirac fermion model

With the DFT data understood, we now proceed to fit our results to the massive Dirac Fermion model (DFM) applicable in the vicinity of K and K' points.

1. Effective massive Dirac fermion model for TMD monolayers

To construct the effective low-energy model for TMD MLs nearby K and K' points, we consider the basis $|\phi_1\rangle = |C, \uparrow\rangle$, $|\phi_2\rangle = |V, \uparrow\rangle$, $|\phi_3\rangle = |C, \downarrow\rangle$ and $|\phi_4\rangle = |V, \downarrow\rangle$, where $C = d_{z^2}$ and $V = \frac{1}{\sqrt{2}}(|d_{x^2-y^2}\rangle + i\tau_i |d_{xy}\rangle)$ are the atomic orbitals of the conduction and valence band edges, and \uparrow, \downarrow represents the z component of the electronic spin. The i th ML Hamiltonian ($i = 1$ for MoS₂ and $i = 2$ for WS₂) can be described by

$$H_{kp}^i(\vec{q}) = H_0^i + H_1^i(\vec{q}) + H_2^i(\vec{q}) + H_3^i(\vec{q}), \quad (1)$$

where H_j^i is the term with j th order in \vec{q} for i th ML TMD, \vec{q} is a wave vector relative to K or K' point in momentum space. The first term in the right-hand side of Eq. (1) is given by

$$H_0^i = E_F 1 \otimes \tilde{1} + 1 \otimes \Delta_i \tilde{\sigma}_+ - \tau_i \sigma_z \otimes (\lambda_{c,i} \tilde{\sigma}_+ - \lambda_{v,i} \tilde{\sigma}_-). \quad (2)$$

σ_z ($\tilde{\sigma}_z$) and 1 ($\tilde{1}$) represent the z -component Pauli matrix ($\hbar = 1$) and the 2×2 identity matrix in spin H_s (pseudospin \tilde{H}) subspace. Furthermore, we define the matrices $\tilde{\sigma}_+$ and $\tilde{\sigma}_-$ as $\tilde{\sigma}_\pm = (\tilde{1} \pm \tilde{\sigma}_z)/2$. Finally, τ_i is the valley index: $\tau_i = +1$ in K valley and $\tau_i = -1$ in K' valley. With the restriction that $\lambda_{v,i}$ is always positive, while $\lambda_{c,1}$ is positive (for Mo-based material) and $\lambda_{c,2}$ is negative (for W-based TMDs), the energy of the fermi level E_F , the energy gap Δ_i , and the spin-orbit splitting in conduction/valence band $\lambda_{c/v,i}$ are obtained by fitting the results of DFM with *first principles* calculation data (see Appendix A for details). The term linear in \vec{q} is given by

$$H_1^i(\vec{q}) = 1 \otimes \gamma_{0,i} a (\tau q_x \tilde{\sigma}_x + q_y \tilde{\sigma}_y). \quad (3)$$

In matrix form, the right hand terms in Eq. (1) are given by

$$H_0^i = \begin{bmatrix} E_{F,i} + \Delta_i - \tau_i \lambda_{c,i} & 0 & 0 & 0 \\ 0 & E_{F,i} + \tau_i \lambda_{v,i} & 0 & 0 \\ 0 & 0 & E_{F,i} + \Delta_i + \tau_i \lambda_{c,i} & 0 \\ 0 & 0 & 0 & E_{F,i} - \tau_i \lambda_{v,i} \end{bmatrix} \quad (4)$$

and

$$H_1^i(\vec{q}) = \begin{bmatrix} 0 & \delta_{0,i}f_1(\vec{q}, \tau_i) & 0 & 0 \\ \delta_{0,i}f_1^\dagger(\vec{q}, \tau_i) & 0 & 0 & 0 \\ 0 & 0 & 0 & \delta_{0,i}f_1(\vec{q}, \tau_i) \\ 0 & 0 & \delta_{0,i}f_1^\dagger(\vec{q}, \tau_i) & 0 \end{bmatrix} \quad (5)$$

with

$$f_1(\vec{q}, \tau_i) = a(\tau_i q_x - i q_y), \quad (6)$$

and

$$H_2^i(\vec{q}) = \begin{bmatrix} \delta_{1,i}f_2(\vec{q}) & \delta_{3,i}f_3(\vec{q}, \tau_i) & 0 & 0 \\ \delta_{3,i}f_3^\dagger(\vec{q}, \tau_i) & \delta_{2,i}f_2(\vec{q}) & 0 & 0 \\ 0 & 0 & \delta_{1,i}f_2(\vec{q}) & \delta_{3,i}f_3(\vec{q}, \tau_i) \\ 0 & 0 & \delta_{3,i}f_3^\dagger(\vec{q}, \tau_i) & \delta_{2,i}f_2(\vec{q}) \end{bmatrix} \quad (7)$$

and

$$H_3^i(\vec{q}) = \begin{bmatrix} \delta_{4,i}f_4(\vec{q}, \tau_i) & \delta_{6,i}f_5(\vec{q}, \tau_i) & 0 & 0 \\ \delta_{6,i}f_5^\dagger(\vec{q}, \tau_i) & \delta_{5,i}f_4(\vec{q}, \tau_i) & 0 & 0 \\ 0 & 0 & \delta_{4,i}f_4(\vec{q}, \tau_i) & \delta_{6,i}f_5(\vec{q}, \tau_i) \\ 0 & 0 & \delta_{6,i}f_5^\dagger(\vec{q}, \tau_i) & \delta_{5,i}f_4(\vec{q}, \tau_i) \end{bmatrix}, \quad (8)$$

with

$$\begin{aligned} f_2(\vec{q}) &= a^2(q_x^2 + q_y^2), \quad f_3(\vec{q}, \tau) = a^2(\tau q_x + i q_y)^2, \\ f_4(\vec{q}, \tau) &= a^3 \tau q_x (q_x^2 - 3q_y^2), \\ f_5(\vec{q}, \tau) &= a^3 (q_x^2 + q_y^2)(\tau q_x - i q_y), \end{aligned} \quad (9)$$

where a denotes the lattice constant; $\delta_{0,i}$, $\delta_{3,i}$, and $\delta_{6,i}$ are the first-order, second-order, and third-order effective hopping parameters, respectively; $\delta_{1,i}$ and $\delta_{2,i}$ correspond to effective mass parameters of conduction and valence bands, respectively; $\delta_{4,i}$ and $\delta_{5,i}$ represent the trigonal warping. All of these parameters are also obtained by the fitting of $\mathbf{k} \cdot \mathbf{p}$ results with the data of *ab initio* calculation.

2. Effective massive Dirac fermion model for MoS₂/WS₂ heterostructures

With the knowledge of the DFM for TMD monolayers, we can extend it to calculate the electronic band structure of the MoS₂/WS₂ heterostructure. It can be realized by adding hopping terms that preserves the spin into two individual ML Hamiltonian. In the basis of

$$\{|C^1, \uparrow\rangle; |V^1, \uparrow\rangle; |C^1, \downarrow\rangle; |V^1, \downarrow\rangle; |C^2, \uparrow\rangle; |V^2, \uparrow\rangle; |C^2, \downarrow\rangle; |V^2, \downarrow\rangle\},$$

the matrix of the Hamiltonian of MoS₂/WS₂ heterostructure read

$$H_{k,p} = \begin{bmatrix} H_{kp}^1(\vec{q}) & 1 \otimes V \\ 1 \otimes V^* & H_{kp}^2(\vec{q}) \end{bmatrix}, \quad (10)$$

where $H_{kp}^i(\vec{q})$ are the 4×4 matrices of the ML Hamiltonian given in Eq. (1) with $i = \{1, 2\}$ and V is

$$V = \begin{bmatrix} t_e & 0 \\ 0 & t_h \end{bmatrix}, \quad (11)$$

where t_e and t_h are the electron and hole hopping parameters, and τ is the valley index, with $\tau_1 = -\tau_2$ for AB staking.

Figure 3(a) shows a comparison of the lowest energy bands around the CB minimum (VB maximum) in the α valley between DFT data and DFM results. Figures 3(b) and 3(c) display a zoom of the layer- and spin-resolved band structures nearby the band extreme, respectively. We notice that our DFM result (dots) fits very well DFT data (solid lines). The fitting parameters are shown in Table I. The hopping energy of holes t_h is two orders of magnitude larger than that of electrons t_e indicating that the VB mixture between two constituent layers is much stronger than that in CB, see Fig. 3(b).

3. Effective massive Dirac fermion model for the MoS₂/WS₂ heterostructure grown on magnetic substrate

In the MoS₂/WS₂ heterostructure grown on magnetic substrate, an effective magnetic field $\vec{J} = J_{ex}\hat{z}$ generated by a magnetic substrate shifts the band energies following the Zeeman effect. Then the single-particle energy in the presence of MPE is equal to the zero-MPE energy plus Zeeman energy correction. For example, at K or K' point, the energy of the n th band is given by $E_{n,\sigma_z,\tau} = E_{n,\sigma_z,\tau}^0 + \frac{1}{2}(\sigma_z g_s + \tau g_o + \tau g_{v,n})\mu_B J_{ex}$, where $E_{n,\sigma_z,\tau}^0$ refers to the energy of single-particle state with spin σ_z in the n th band of α valley ($\tau = 1$) or β valley ($\tau = -1$) at $J_{ex} = 0$. It is obtained by DFM for

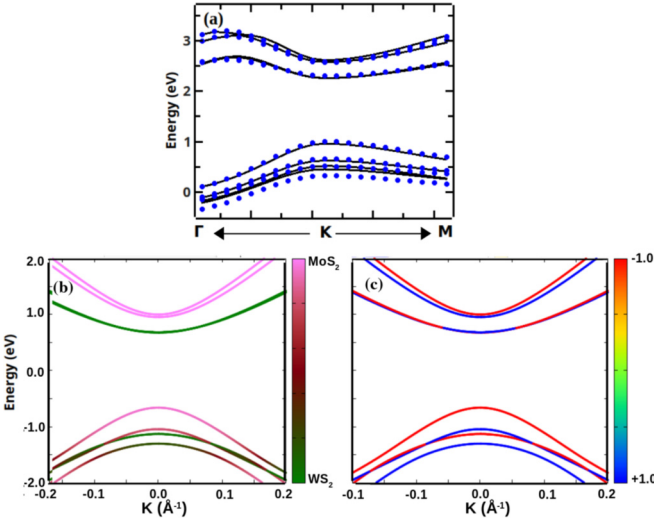


FIG. 3. (a) Comparison of the electronic band structure nearby the K point of MoS₂/WS₂ heterostructure with AB stack obtained by DFT (lines) and the DFM (dots). [(b),(c)] Zoom around the band extremes in α valley. The color codes indicate (b) layer and (c) spin, respectively.

MoS₂/WS₂ heterostructures as, see Sec. II B 2. μ_B is the Bohr magneton, J_{ex} is the exchange field (in Tesla), g_s , g_o , and $g_{v,n}$ stand for the spin, orbital angular moment, and valley g factors, respectively. $g_s = 2$, $g_o = 0$ for CBs and $g_o = 4$ for VBs, and the values of $g_{v,n}$ with $n = c, v$ depend on the Berry curvature (the detailed information is described in Sec. II C).

C. Berry curvature

In solid state physics, the crystal symmetry rules the electronic band structure, as well as the nature of the Bloch states. For the crystal with inversion symmetry, the Berry curvature and valley magnetic moment of the Bloch states are zero [39]. Nevertheless, in crystals with inversion asymmetry such as the WS₂/MoS₂ vdWs heterostructure, they are nonzero [39–41]. Moreover, time-reversal symmetry requires all Berry-phase related physical quantities to be valley-contrasting. However, the presence of an external magnetic or exchange field breaks time-reversal symmetry, and the valley magnetic momentum generates different energy shifts in the two valleys. This pro-

TABLE I. Parameters of DFM for the MoS₂/WS₂ heterostructure with AB stacking.

MoS ₂ /WS ₂	MoS ₂ (eV)		WS ₂ (eV)	
$E_{F,i}$ (eV)	0.7667	Δ_1 1.5572	Δ_2 1.8131	
t_e (eV)	0.0010	$\lambda_{c,1}$ 0.0030	$\lambda_{c,2}$ -0.0069	
t_h (eV)	0.1500	$\lambda_{v,1}$ 0.0740	$\lambda_{v,2}$ 0.1890	
a (Å)	3.18	$\delta_{0,1}$ 1.0502	$\delta_{0,2}$ 1.3849	
		$\delta_{1,1}$ 0.0227	$\delta_{1,2}$ 0.1083	
		$\delta_{2,1}$ 0.0745	$\delta_{2,2}$ 0.0550	
		$\delta_{3,1}$ 0.0016	$\delta_{3,2}$ 0.1082	
		$\delta_{4,1}$ -0.0164	$\delta_{4,2}$ -0.2443	
		$\delta_{5,1}$ -0.1620	$\delta_{5,2}$ 0.0022	
		$\delta_{6,1}$ -0.2287	$\delta_{6,2}$ -0.2540	

vides the remarkable possibility of tuning valley splitting for exploring different external mechanisms.

To gain further insight into the valley dynamics of the interlayer exciton, let us first explore the spin (and valley) Berry curvature $\Omega_n(\mathbf{k})$ and the magnetic moment $m_n(\mathbf{k})$. These two quantities can be calculated by the following general expressions [39,42,43]:

$$\Omega_n(\mathbf{k}) = \mathbf{i} \langle \nabla_{\mathbf{k}} \mathbf{u}_n | \times | \nabla_{\mathbf{k}} \mathbf{u}_n \rangle, \quad (12)$$

$$m_n(\mathbf{k}) = -\mathbf{i} \frac{e}{\hbar} \langle \nabla_{\mathbf{k}} \mathbf{u}_n | \times (\mathbf{H}_{\mathbf{k},p} - E_n) | \nabla_{\mathbf{k}} \mathbf{u}_n \rangle,$$

where $|u_n\rangle$ and E_n are the n th Bloch state and its corresponding energy of the effective Hamiltonian $H_{\mathbf{k},p}$, and k is components of wavevector \mathbf{k} . In the framework of DFM, we have performed numerical calculations to obtain the low-energy band structure. Once the energy bands and the wavefunctions are obtained, the $\Omega_n(\mathbf{k})$ and $m_n(\mathbf{k})$ are calculated using Eq. (12) [44,45]. For example, the valley magnetic moments for the uppermost VB and the lowest CB at $k = 0$ in α valley of the MoS₂/WS₂ heterostructure are given by $m_v = 3.11\mu_B$, $m_c = -1.57\mu_B$ [45]. Then the Zeeman shift due to the valley magnetic moment $m_i(\mathbf{k})$ is evaluated by, $\Delta_{i,\tau} = \tau m_i(\mathbf{k}) B$ with $m_i(\mathbf{k}) = g_{v,i}\mu_B$, $i = c, v$. $g_{v,c}$ and $g_{v,v}$ are the valley angular momentum of the lowest CB and the uppermost VB of the heterostructure, respectively. The valley magnetic moment is a major contributor to exciton g factors and Zeeman shift. This is due to the fact that in the heterostructure with AB stacking, the IX in α valley constitutes an electron in CB of K -valley of WS₂ and a hole in VB of the K' valley of MoS₂. Thus the valley magnetic moment contribution to the g factor of IX excitons will be proportional to $g_{v,c} + g_{v,v}$.

D. Valley dynamics of interlayer excitons

In analogy to the valley physics of intralayer exciton in TMD monolayers [46], the VP of the IXs can also be injected via optical excitation. For example, for nonmagnetic vdWs heterostructures, one usually resorts to the circularly polarized light excitation to get a VP injection. In contrast, for the magnetic MoS₂/WS₂ heterostructures, either circularly or linearly polarized lights can be used as pumping light sources. In both cases, the detection is performed using a circular polarization basis. Since there are both the intralayer relaxations and inter-valley scatterings channels, the optically injected VP changes. With the low-energy model in hand, we are ready to study the exciton dynamics and VP for the MoS₂/WS₂ heterostructure in the presence of a magnetic substrate.

1. Four band model

To get a better grasp of the underlying physics of IXs dynamics in MoS₂/WS₂ heterostructure with AB stacking and magnetic substrate, we start by the four bands model shown in Fig. 4. The parabolic bands in panel (a) represent schematically the band structure around the α and β points of MoS₂/WS₂ heterostructure. The IXs, labeled by $|3\rangle$ and $|3'\rangle$ in α and β valleys are also shown. To accurately describe the intra- and interlayer exciton dynamics, we start with a simple case in which the bright (spin allowed) intralayer A exciton in WS₂ is optically excited and may (i) perform an

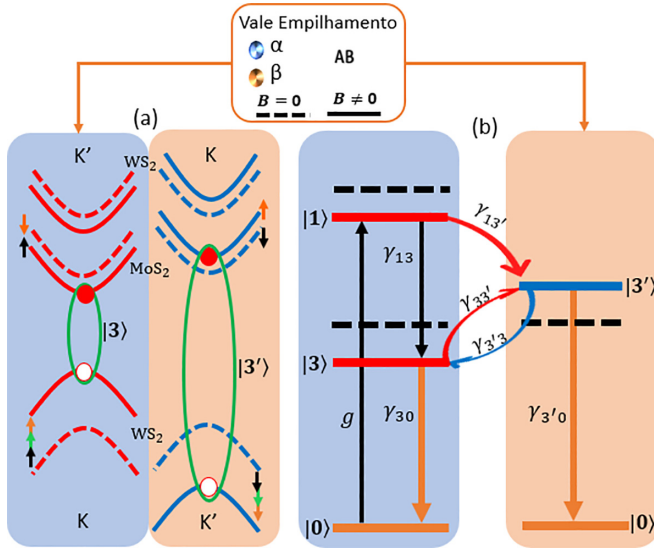


FIG. 4. Schematic diagrams of (a) the electronic band structure around energy band extremes and (b) exciton energy levels and the corresponding scatterings of MoS₂/WS₂ heterostructure with AB stacking configuration. The blue and orange rectangles are designated for α and β valleys, respectively. Solid (dashed) lines correspond to the energy levels in the presence (absence) of exchange field. The black, green, and orange arrows in (a) represent spin, angular momentum, and valley magnetic moments, respectively. In (b), vertical arrows illustrate intravalley transitions and relaxations, while the slanted arrows indicate intervalley scatterings. The corresponding transition rates are given by γ_{ij} (nearby the arrows). $|0\rangle$ is the ground state, $|1\rangle$ ($|1'\rangle$) and $|3\rangle$ ($|3'\rangle$) are intralayer and interlayer exciton states in α (β) valley, respectively.

intravalley scattering to the low-energy interlayer bright state or (ii) generate an interlayer exciton in K' valley via intervalley scattering. They can recombine via radiative processes, or go through intravalley and intervalley scatterings. Such scattering processes are displayed in Fig. 4(b), where arrows represent optical excitation, optical recombination, and exciton scatterings. The exciton bands are shown by the horizontal lines. $|1\rangle$ and $|3\rangle$ label the DX and IX states in α valley, respectively, while $'$ refers to their counterpart in the β valley. Dotted lines refer to the valley-degenerate exciton states in the absence of an external magnetic field, while solid horizontal lines represent the excitonic states in the presence of the exchange field. Notice that the shifts of the exciton states are opposite in α and β valleys.

The relaxations and scattering processes in Fig. 4(b) are described by the following coupled rate equations:

$$\begin{aligned} \dot{n}_1 &= g - \gamma_{13}n_1 - \gamma_{13'}n_1', \\ \dot{n}'_1 &= \gamma_{13'}n_1 - \gamma_{3'3}n'_3 + \gamma_{33'}n_3 - \gamma_{3'0}n'_3, \\ \dot{n}_3 &= \gamma_{13}n_1 + \gamma_{3'3}n'_3 - \gamma_{33'}n_3 - \gamma_{30}n_3, \\ n_0 + n_1 + n_3 + n'_3 &= 1, \end{aligned} \quad (13)$$

where n_j (n'_j) represents the exciton density in the $|j\rangle$ state in the α (β) valley. In particular, n_0 denotes the density in the ground state (vacuum). γ_{ij} stands for the scattering rate from state i to j . In Eq. (13), we assume that the optical excitation is in resonance with the A exciton in WS₂ of α

valley with photon generation rate g , see Fig. 4. To compute the steady-state PL intensity, we solve the coupled rate equations with $\dot{n}_j = 0 \forall j$. The PL intensity of the j th state can then be obtained via $I_j = \gamma_{j0}n_j$. With the values of IX emission intensities in two valleys at hand, the degree of valley polarization can be evaluated via $VP = (I^+ - I^-)/(I^+ + I^-)$, where the I^+ and I^- stand for the PL intensities of IXs in the α and β valleys, respectively. Therefore, the VP of IX emission is evaluated as $VP = (I_3 - I_{3'})/(I_3 + I_{3'})$, where I_3 and $I_{3'}$ denote the PL intensity of IX in α and β valleys, respectively. Solving Eq. (13) with $\gamma_{30} = \gamma_{3'0} = \gamma$ we found

$$VP = P_0 \frac{\gamma}{\gamma + \gamma_{33'} + \gamma_{3'3}} + \frac{\gamma_{33'} - \gamma_{3'3}}{\gamma + \gamma_{33'} + \gamma_{3'3}}. \quad (14)$$

The first term in Eq. (14) is related to the optically created polarization where P_0 is defined by $P_0 = (\gamma_{13} - \gamma_{13'})/(\gamma_{13} + \gamma_{13'})$, which is the polarization injected from the circularly polarized excitation through generation of the DX, interlayer charge transfer and IX formation. The second term describes the tendency of the system to reach thermal equilibrium, dictated by the MPE tuned intervalley scattering.

2. Five band model

In the last section, we have introduced a simple model to describe IX dynamics in the MoS₂/WS₂ heterostructures excited by circularly polarized light. Now, we extend our study by incorporating extra scattering channels, to the system excited by either circularly or linearly polarized lights (see Fig. 5). Besides the charge transfer and intervalley scattering, we consider that the photogenerated intralayer exciton may also (i) recombine radiatively (rate γ_{10}) or scatter to state $|1'\rangle$, the intralayer exciton in K' valley (rate $\gamma_{11'}$). The scatterings and relaxation processes shown in Fig. 5 are described by the set of equations below:

$$\begin{aligned} \dot{n}_1 &= g - (\gamma_{10} + \gamma_{13} + \gamma_{13'} + \gamma_{11'} + \gamma_{nr})n_1 + \gamma_{11'}n'_1, \\ \dot{n}'_1 &= g' - (\gamma_{1'0} + \gamma_{1'3'} + \gamma_{1'3} + \gamma_{1'1} + \gamma_{nr'})n'_1 + \gamma_{11'}n_1, \\ \dot{n}_3 &= -(\gamma_{30} + \gamma_{33'} + \gamma_{nr})n_3 + \gamma_{13}n_1 + \gamma_{1'3}n'_1 + \gamma_{3'3}n'_3, \\ \dot{n}'_3 &= -(\gamma_{3'0} + \gamma_{3'3} + \gamma_{nr'})n'_3 + \gamma_{1'3}n'_1 + \gamma_{33'}n_3 + \gamma_{13}n_1, \end{aligned} \quad (15)$$

where we have used the same notation as that in Eqs. (13). It is worth remarking that our exciton dynamics model is highly flexible and the number of parameters involving in rate equations is controllable. From the models of four and five bands, the exciton dynamic model can be easily extended or simplified by adding or removing the number of scattering channels, leading to a controllable number of parameters involving in rate equations. In addition, all relevant parameters adopted in the calculations are either evaluated from our atomistic simulation or taken from experimental data, ensuring the validity of our theoretical outcomes about PL intensity and valley polarization.

3. Scattering parameters

As discussed in the previous sections, the dynamics of DX and IX is composed of radiative relaxation processes described by γ_{10} and γ_{30} in α valley and $\gamma_{1'0}$ and $\gamma_{3'0}$ in β

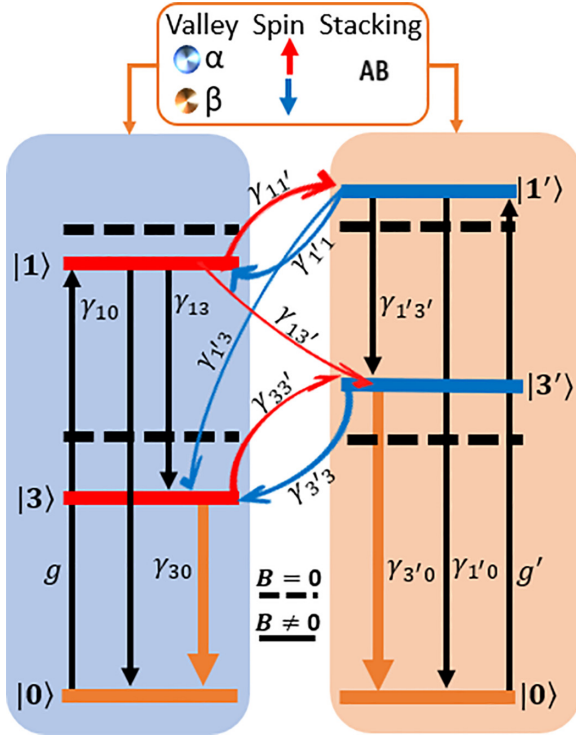


FIG. 5. Schematic representation of five band model of IX dynamics in the MoS₂/WS₂ heterostructure. The blue and orange rectangles are designated for α and β valleys, respectively. Horizontal-solid (dashed) lines represent exciton energy levels with (without) exchange field. Vertical arrows indicate intravalley transitions and relaxation processes, while the slanted arrows indicate intervalley scatterings. The Greek alphabet γ_{ij} nearby the arrows stand for the corresponding transition rates. $|0\rangle$ is the ground state, $|1\rangle$ ($|1'\rangle$) and $|3\rangle$ ($|3'\rangle$) are intralayer and interlayer exciton states in α (β) valley, respectively.

valley, and interlayer charge transfer process characterized by γ_{13} , $\gamma_{1'3'}$, $\gamma_{13'}$, and $\gamma_{1'3}$. To calculate radiative relaxation parameters, we start by fitting the $\mathbf{k} \cdot \mathbf{p}$ model with the DFT data to get single-particle wavefunctions and energies, latter we include exciton quasiparticles. After that the radiative lifetimes of intralayer excitons in monolayer TMDs are obtained using Fermi's golden rule [47]. With the radiative lifetimes of the intralayer excitons at hand, the corresponding values of IXs can be eventually calculated using low-energy approximation, see the Appendix B. In the absence of exchange field, we obtain $(\gamma_{10})^{-1} = (\gamma_{1'0})^{-1} = 4.27$ ps and $(\gamma_{30})^{-1} = (\gamma_{3'0})^{-1} = 1634$ ps at $T = 4.5$ K. In addition, the radiative lifetimes of IXs depend strongly on the exchange field J_{ex} [29], dictated by the following relations: $\gamma_{10} = (2.85e^{(-J_{ex}/6.29T)} + 1.42)^{-1}$ ps⁻¹ and $\gamma_{30} = (1089e^{(-J_{ex}/6.29T)} + 545)^{-1}$ ps⁻¹, respectively [29]. We assume that the $\gamma_{1'0}$ ($\gamma_{3'0}$) has a similar dependence on J_{ex} with that of γ_{10} (γ_{30}). Besides the radiative relaxations, we also consider nonradiative relaxation processes with scattering rate $\gamma_{nr} = (1 \text{ ns})^{-1}$ for both intra and interlayer excitons.

Concerning the scattering between different excitonic states, the intravalley charge transfer channel from $|1\rangle$ to $|3\rangle$ is one relaxation process between two like-spin states, while the inter-valley charge transfer channel from $|1\rangle$ to $|3'\rangle$ takes place

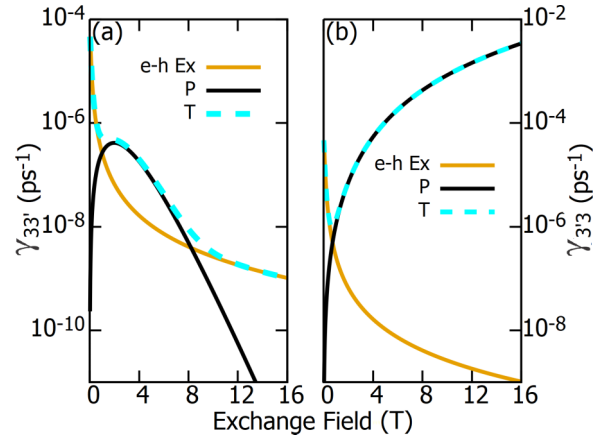


FIG. 6. Intervalley scattering rates of (a) $\gamma_{33'}$ and (b) $\gamma_{3'3}$ as a function of exchange field for $\alpha = 5 \times 10^3$ ps⁻¹eV⁻³. $e-h$ and P represent, respectively, the intervalley scattering rates due to the electron-hole exchange interaction and phonon-assisted processes. T stands for the scattering rate for the case involving these two scattering channels.

in antiparallel spin states. Typically, the transition rate of the former is larger than that of the latter. The quantitative relationship among these scattering parameters can be described as follows: $\gamma_{13'} = \gamma_{13}(1 + P_{03})/(1 - P_{03})$ with $\gamma_{13} = \gamma_{1'3'} = 1/70$ ps⁻¹ [48] and $P_{03} = -0.29$ [29]. With this choice, we have $\gamma_{13} > \gamma_{13'}$.

For the definition of $\gamma_{jj'}$, we consider the two major intervalley scattering mechanisms: the electron-hole exchange interaction and the phonon-assisted intervalley scattering [49–51]. The electron-hole exchange interaction acts as an effective in-plane magnetic field, leading to the precession of the valley pseudospin. This pseudospin precession together with its reorientation due to momentum scattering constitutes a net change of pseudospin states. Because this is a resonant process, it is only effective when the two states in different valleys are close in energy. At zero exchange field, VP is mainly dictated by this mechanism. At finite exchange field, however, J_{ex} lifts the degeneracy, suppressing intervalley scatterings induced by electron-hole exchange interaction. With increasing J_{ex} , this tendency becomes more and more pronounced. In contrast, the phonon-assisted intervalley scattering between two Zeeman split states becomes relevant [acoustical chiral phonons play an important role here since the VS is of the order of few meV, see Fig. 7(c)], resulting in an exciton population imbalance in the two valleys. With further increasing J_{ex} , it will become a dominant relaxation process. This mechanism depends strongly on exciton-phonon coupling strength α_{ph} . Considering both mechanisms, the intervalley scattering rate $\gamma_{jj'}$ from state j to state j' has the form

$$\gamma_{jj'} = \frac{1}{\tau_{v0}^{jj'}} \frac{\Gamma^2}{\Gamma^2 + (\Delta E_{jj'})^2} + \frac{\alpha_{ph} |\Delta E_{jj'}|^3}{\left| \exp\left(\frac{\Delta E_{jj'}}{k_B T}\right) - 1 \right|}, \quad (16)$$

where $\tau_{v0}^{jj'}$ and α_{ph} are adjustable parameters representing the strengths of zero field intervalley scattering and the exciton-phonon coupling, Γ is a width, which may be related to the exciton momentum relaxation. $\Delta E_{jj'} = E_{j'} - E_j$ is the valley unfolding of the exciton state with $j = \{1, 3\}$ and $j' =$

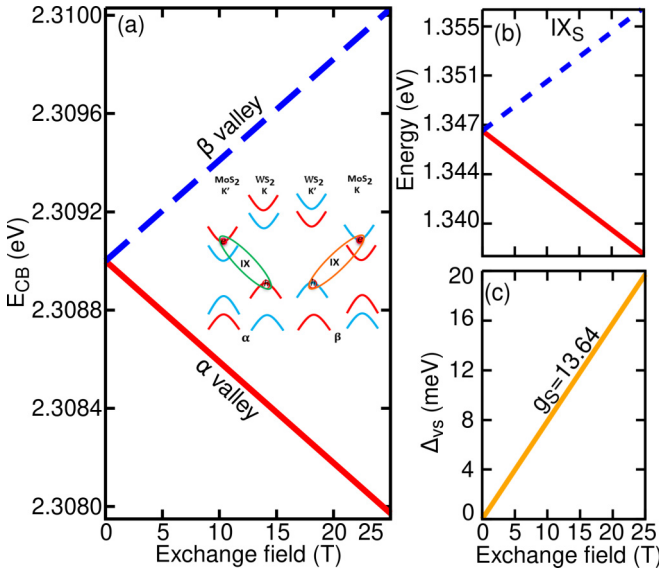


FIG. 7. (a) Single-particle energy at CBM in α (red) and β (blue) valleys. Inset shows schematically the formations of the IXs in α (left) and β (right) valleys, see the electron-hole pairs inside ellipses. K and K' refer to the valleys of the individual monolayer TMDs. (b) Exciton energy in α (red) and β (blue) valleys. (c) Valley splitting VS, defined by $\Delta_{vs} = |E_{\sigma^+} - E_{\sigma^-}|$, where E_{σ^+} and E_{σ^-} denote PL peak positions of σ^+ emission in α valley and σ^- emission in β valley, respectively. These VSs correspond to an effective g factor of the IX being equal to 13.64.

$\{1', 3'\}$. The first term in Eq. (16) describes the effect of the electron-hole exchange interaction on intervalley scattering. The second term is the standard form for the direct phonon-induced spin-lattice scattering, which demands either the absorption ($E_j > E_j$) or emission ($E_j < E_j$) of a phonon. For the case of zero-exchange field, the time reversal symmetry requires $\gamma_{33'} = \gamma_{3'3}$. Then the second term becomes zero. The VP reduces to the well-known expression for optically created PL polarization, i.e., $VP = P_0/(1 + \tau_r/\tau_v)$, where $\tau_r = 1/\gamma$ is the recombination time, while $\tau_v = 1/(\gamma_{21} + \gamma_{12})$ is the intervalley scattering time. Making the fitting shown in Fig. 8, we obtain the parameters $\Gamma = 40 \mu\text{eV}$, $\alpha_{ph} = 3 \times$

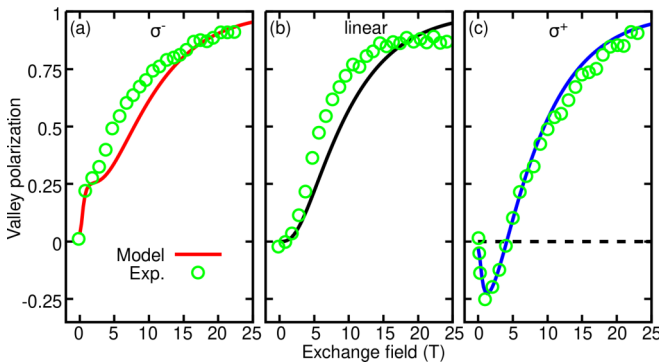


FIG. 8. VP of IX emissions in $\text{MoS}_2/\text{MoSe}_2/\text{MoSe}_2$ heterostructure as a function of out of plane magnetic field for (a) σ^- , (b) linearly, and (c) σ^+ polarized excitations. Solid-blue lines correspond to our theoretical prediction, while the red circles are experimental data from reference [29].

$10^5 \text{ ps}^{-1} \text{ eV}^{-3}$ and the intervalley relaxation time for the zero field, $\tau_{v0} = 40 \text{ ns}$, four orders of magnitude larger than the exciton in the $\text{WSe}_2/\text{MoSe}_2$ heterostructure.

Figure 6 depicts the contributions of different scattering mechanisms to the intervalley scattering rates of (a) $\gamma_{33'}$ and (b) $\gamma_{3'3}$ as a function of J_{ex} for σ^+ excitation. At zero-exchange field, the exciton states are valley degenerate. The scattering is dominated by the electron-hole Coulomb exchange interaction. An application of the exchange field lifts the valley degeneracy, lowering the state in α valley relative to its counterpart in β valley. This energy difference suppresses the intervalley scattering originating from electron-hole exchange Coulomb interaction, for both the forward (from $|3\rangle$ to $|3'\rangle$) and backward (from $|3'\rangle$ to $|3\rangle$) scatterings, see yellow curves. On the other hand, the phonon-assisted intervalley scatterings start to play a part in VP. As the exchange field increases, the scattering rate initially increases due to usual mechanism of exciton-phonon coupling. At $J_{ex} = 3.2 \text{ T}$, the forward scattering rate reaches its maximum. After that, the forward and backward scattering rates exhibit an opposite exchange field dependence. It is attributed to the valley splitting, as shown in Fig. 5. Because the energy of $|3'\rangle$ is larger than that of $|3\rangle$, the phonon-assisted backward (forward) process is energetically favorable (unfavorable). Then the scattering rate of the former goes up, while the latter goes down. Hence there are two scattering regimes. In the regime of small J_{ex} , the usual phonon induced intervalley scattering plays an important role. Nevertheless, for large J_{ex} , the phonon-assisted intervalley scattering dominates the process. Hence, unlike usual phonon scatterings, which are always harmful to VP such as phonon involved scatterings in pristine TMDs or TMD heterostructures. In magnetic vdWs heterostructures, the MPE enhances the scattering from the valley with a higher energy to the one with a lower energy and suppresses its backward scattering. In addition, the interplay between the two intervalley scattering mechanisms, i.e., electron-hole exchange interaction and phonon, gives rise to a monotonic reduction of total intervalley scattering rate in α valley and a nonmonotonic increase in β valley. All the parameters described above are summarized in Appendix C.

III. RESULTS AND DISCUSSION

MPE causes a shift of the energy bands of vdW heterostructure, which can be calculated taking into account the overall contribution of the spin, orbital and valley components. The quantitative dependence of the electronic structure on J_{ex} can be obtained by exact diagonalization or by low-energy approximation ($\mathbf{k} \cdot \mathbf{p}$ model). The calculations follow the convention: τ is +1 in the K valley and -1 in the K' valley for either MoS_2 or WS_2 ML. In the MoS_2/WS_2 heterostructure with AB stacking, the α valley is composed of the K valley of WS_2 and the K' valley of ML MoS_2 , while the β valley possesses time reversal symmetry with the α valley, see the inset of Fig. 7(a). Figure 7(a) shows the exchange field dependence of single-particle energy at CB minimum in α (red) and β (blue) valleys. Because spin and valley magnetic moments have opposite signs in α and β valleys, the corresponding single-particle energy levels experience an opposite

Zeeman shift. Therefore, nonzero J_{ex} lifts valley degeneracy of single-particle states, yielding finite VSs.

Unlike the single-particle state, the IX is a two particle state involving an electron and a hole in different layers. For instance, the IX in α valley is comprised of an electron in K' valley of MoS_2 and a hole in K valley of WS_2 , see the inset in Fig. 7(a). Since the involved conduction and valence band states of the exciton are the same spin states, its energy E_3 is determined by

$$E_3 = E_{3,0} - \frac{1}{2}(g_{v,v} + g_{v,c} + g_o)\mu_B J_{ex}, \quad (17)$$

where $E_{3,0}$ is the zero-field energy of IX. On the other hand, the IX in β valley consists of an electron in K valley of MoS_2 and a hole in K' valley of WS_2 , see the inset in Fig. 7 (a). Then its energy reads $E_{3'} = E_{3,0} + \frac{1}{2}(g_{v,v} + g_{v,c} + g_o)\mu_B J_{ex}$. Figure 7(b) shows the energies of IXs as a function of J_{ex} . We observe that as J_{ex} increases, the energy of IX in α valley decreases, while it increases in β valley. To relate our theoretical predictions with experimental measurements, let us introduce valley splitting Δ_{vs} , defined by $\Delta_{vs} = |E_{\sigma^+} - E_{\sigma^-}|$, where E_{σ^+} (E_{σ^-}) denotes PL peak position of σ^+ (σ^-) emission in α (β) valley, i.e., $E_{\sigma^+} = E_3$ and $E_{\sigma^-} = E_{3'}$. Then VS reads, $\Delta_{vs} = (g_{v,v} + g_{v,c} + g_o)\mu_B J_{ex}$, namely, VS depends linearly on the exchange field, as shown in Fig. 7(c). The corresponding exciton g factor is equal to $g = 13.64$. The giant VS and g factor of the IX can be understood as follows. Since the IX states involve conduction and valence band same spin states, the coupling of field to the spin angular momentum shifts the conduction and valence bands by the same amount, which does not contribute to the emission energy. Nevertheless, unlike the intralayer exciton, the Zeeman energy due to valley magnetic moment does contribute to VS. Because the valley magnetic moment of the electron in MoS_2 layer has an opposite sign to that of the hole in WS_2 layer, the shift of CB is along an opposite direction to the shift of VB. Then the VS is a sum over absolute values of these two energy shifts. Similar behavior of the Zeeman shift is found for the orbital angular momentum. Then the total VS is equal to the one induced by orbital magnetic moment plus the other caused by the valley magnetic moment. Based on the VS, we can straightforwardly calculate the effective g factor of the IXs via $g = \Delta_{vs}/(\mu_B J_{ex})$, i.e., $g = g_{v,v} + g_{v,c} + g_o = 13.64$, where $\mu_B \sim 58 \mu\text{eV/T}$ is the Bohr magneton.

Unless otherwise specified, we assume that the magneto-PL is excited by either circularly or linearly polarized light with the excitation photon energy in resonance with the A exciton in the WS_2 , and it is detected using a circular polarization basis. We also suppose that the system is in the Faraday geometry, i.e., an out of plane J_{ex} is exerted by magnetic proximity effect.

To validate our theoretical model, a comparison between the results obtained by our rate equations [Eq. (15)] (solid lines) and that measured by magneto-PL spectroscopy (green circles) of $\text{MoS}_2/\text{MoSe}_2/\text{MoS}_2$ heterostructure grown on ferromagnetic substrate is shown in Fig. 8. The panels (a), (b), and (c) display the exchange field dependent VP of IX emissions under σ^- , linearly, and σ^+ polarized light excitations. Our theoretical prediction for the VP of the IX is in very good agreement with experimental data [29]. Three distinct regimes are clearly observed. In the regime of low exchange

field ($J_{ex} < 5T$), the VP exhibits an optical excitation dependence. For example, in (c), the VP hosts an opposite sign to those shown in (a) and (b), and it is also opposite to the polarization of corresponding excitation laser. It is attributed to interplay between electron-hole exchange interaction and phonon-mediated intervalley scatterings. At zero-exchange field, the valley polarization degree is mainly determined by the former, which takes place between two-degenerated states in K and K' valleys. A small VP is observed. In the presence of an exchange field, a lifting of the valley degeneracy, in one hand, suppresses efficiently the electron-hole exchange interaction induced scattering channel, resulting in a recovery of the optically induced VP. On the other hand, it promotes the phonon-assisted intervalley scattering between Zeeman split levels, resulting in a population imbalance in two valleys. The bigger the J_{ex} , the larger the VS and the more pronounced the phonon-assisted intervalley scattering. Then in the regime of small J_{ex} , the VP of IX emission exhibits an excitation laser helicity dependent behavior. As J_{ex} increases, the phonon-assisted intervalley scattering plays more and more important role in the optical process. Eventually, it becomes a dominated scattering mechanism. As a result, a VP due to the thermal occupation of valley Zeeman split states increases. Figure 8 shows that in the interval of $5 \sim 20$ T, all of VPs at three different excitation conditions (σ^- , σ^+ , and linear) increase with increasing J_{ex} , independent of the injected optical polarization. For $J_{ex} > 20$ T, they reach their saturation values. It is worthwhile to mention that because of the unavailability of relevant MoS_2/WS_2 experimental data in the literature, we performed a curve fitting to the magneto-PL data of $\text{MoS}_2/\text{MoSe}_2/\text{MoS}_2$ heterostructure. As expected, a bit difference between the physical parameters of $\text{MoS}_2/\text{MoSe}_2$ and MoS_2/WS_2 heterostructures leads to a slight deviation of our fitting curves from the experimental data. It is also interesting to point out that to properly fit the experimental data of $\text{MoS}_2/\text{MoSe}_2/\text{MoS}_2$ heterostructure, the effects of the Moiré pattern on the intervalley scattering rate is accounted, which yields the VP of IX emissions opposite to the polarization of the excitation beam (see the negative polarization for σ^+ excitation at low field) [29]. In the systems in which there is no moiré pattern such as our MoS_2/WS_2 heterostructure with AB stacking, however, copolarized IX emissions are expected.

Figure 9 shows exchange-field evolution of PL spectrum of the IX in the MoS_2/WS_2 heterostructure grown on ferromagnetic substrate under σ^+ polarized light excitations for the intervalley scattering time τ_{13} equal to (a) 70 and (b) 0.07 ps, respectively. The PL signal from α and β valleys can be detected separately by circularly polarized light detectors. At $J_{ex} = 0$, a single emission peak is found due to the valley degeneracy of $|3\rangle$ and $|3'\rangle$. The out of plane J_{ex} breaks the time reversal symmetry of the heterostructure and lifts the valley degeneracy. As a result, the single emission peak at $J_{ex} = 0$ splits into two peaks, corresponding to the IX emissions in the α and β valleys. An increasing of J_{ex} causes a red-shift of the former, while a blue shift of the latter, giving rise to an increased VS, see the dashed green lines. Interestingly, because of a large exciton g factor, the VS is more than three times bigger than that of the intralayer bright exciton. In addition, this large VS leads to a sizable imbalance

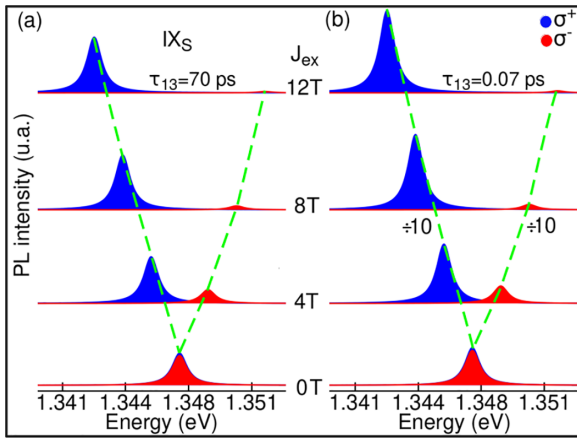


FIG. 9. Exchange field dependence of IX emission spectra in the MoS_2/WS_2 heterostructure grown on ferromagnetic substrate under σ^+ polarized excitations at a pumping laser power $P = 1 \text{ kW/cm}^2$ for (a) $\tau_{13} = 70$ and (b) 0.07 ps, respectively. The blue and red PL peaks refer to the emissions from α valley (σ^+ detection) and β valley (σ^- detection), respectively. The PL intensities in (a) are scaled by a factor of 10 for visibility. The dashed lines only guide to eye.

of exciton population in the two valleys. Then the blue peak becomes fostered, accompanying by the red one being gradually suppressed. Interestingly, this behavior can be effectively tailored by the interlayer charge transfer rate τ_{13} . The rapid charge transfer (smaller τ_{13}) promotes an enhancement of the IX emissions in α and β valleys and a large difference between their PL intensities, yielding a giant VP. Because the charge transfer rate could be conveniently tuned either by an applied vertical gate voltage or by intercalation between two constituent monolayers, it opens a fascinating novel pathway for tuning VP [41,52–54].

In order to gain a deep insight into IX emission, in the following, let us make a systematic investigation about the dependence of IX emission intensity and VP on the interlayer charge transfer rate and exchange field. Figure 10 shows PL intensity of the IX, excited by σ^- laser field in resonance with β valley A exciton of WS_2 as a function of exchange field for different charge transfer rate ($=\tau_{13}^{-1}$). Solid and dashed lines correspond to the σ^+ and σ^- emissions, occurring in α and β valleys, respectively. We note that at $J_{ex} = 0$, the PL intensity of IX emission in α valley is smaller than that in β valley, i.e., the VP is negative. With a reduction of τ_{13} , the difference of PL intensity between them is significantly enlarged. This indicates that the fast charge transfer process from the WS_2 layer to MoS_2 layer produces an imbalance of exciton populations in α and β valleys. The underlying physics is as follows. Optical excitation creates the intralayer excitons in the WS_2 monolayer. Because of type-II band alignment of the system, the photogenerated electrons in WS_2 layer are rapidly transferred to MoS_2 layer. Then the IX, a bound state of electron-hole pair, forms. There are two interlayer charge transfer channels. One is from $|1\rangle$ to $|3\rangle$ and the other is from $|1\rangle$ to $|3'\rangle$. The former is a process between two like-spin states, while the latter is an unlike-spin relaxation process. The relaxation rate of the former process is larger than that of the latter. Then the VP of IX emission is negative. To

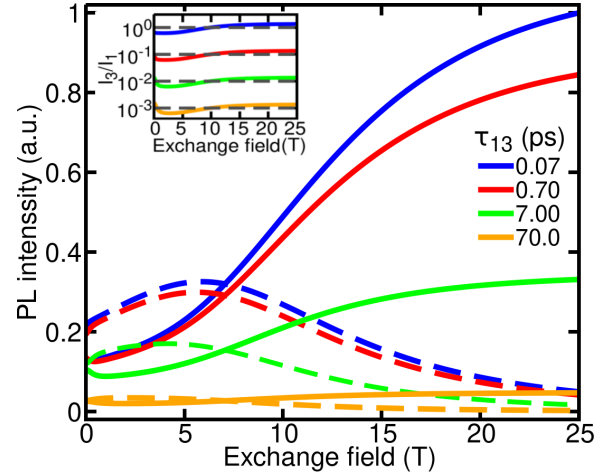


FIG. 10. PL intensity of IX emissions in MoS_2/WS_2 heterostructure on insulator magnetic substrate, excited by σ^- laser field, as a function of exchange field for different values of interlayer charge transfer rate (τ_{13}^{-1}). Solid and dotted lines correspond to the IX emissions in α and β valleys, respectively. Inset: ratio of IX to DX PL intensities for different values of τ_{13} . Results obtained with $\alpha_{ph} = 5 \times 10^3 \text{ ps}^{-1} \text{ eV}^{-3}$ at $T = 4.5 \text{ K}$.

quantitatively describe these two charge transfer processes, $\gamma_{13'} = \gamma_{13}(1 - P_0)/(1 + P_0)$ with $P_0 = -0.29$ is used. Thus a reduction of τ_{13} leads to an increase of both γ_{13} and $\gamma_{13'}$ as well as their difference. Therefore, the PL intensity of the σ^+ and σ^- emissions is enhanced. Moreover, the difference between them also becomes bigger. For finite J_{ex} , the PL intensity of IX emission also exhibits a strong dependence on charge transfer rate. For a given value of τ_{13} , as the J_{ex} increases from zero, the PL intensity in α valley initially decreases till reaches its minimum. After that the PL intensity starts to increase. As a compensation for the this change, the PL intensity in β valley initially increases till reaches its maximum value. After that it falls down. This opposite behavior leads to a crossover between the curves of PL intensity in α and β valleys. Consequently, the sign of the VP switches from a negative to positive value. Interestingly, a critical point ($J_{ex} = J_c$) where this switch occurs is tunable by τ_{13} . As τ_{13} decreases, the critical point moves to higher exchange field side. In addition, both the J_{ex} and τ_{13} enlarge the VP at critical point. Remarkably, the ratio of I_3 and I_1 can be amplified as high as four orders of magnitude when τ_{13} is shortened from 70 to 0.07 ps, see the inset.

With an understanding of the effects of the charge transfer rate, let us turn our attention to manipulation of the IX emission by the exciton-phonon coupling strength (α_{ph}). Figure 11 displays the dependence of the IX PL intensity on the exchange field for different α_{ph} at $\gamma_{13} = (70 \text{ ps})^{-1}$ under (a) σ^+ ($g \neq 0, g' = 0$), (b) linear ($g = g' \neq 0$), and (c) σ^- ($g = 0, g' \neq 0$) light excitations. Solid and dashed curves represent the PL intensities of IX emissions in α and β valleys, respectively. As known, for a circularly polarized excitation, the VP of intralayer exciton at zero exchange field might be nonzero due to the valley-selective circular dichroism of the monolayer TMDs. Because the MoS_2/WS_2 heterostructure inherits valley-selective circular dichroism from its constituent monolayers, the PL intensity of IX emission in α valley is different

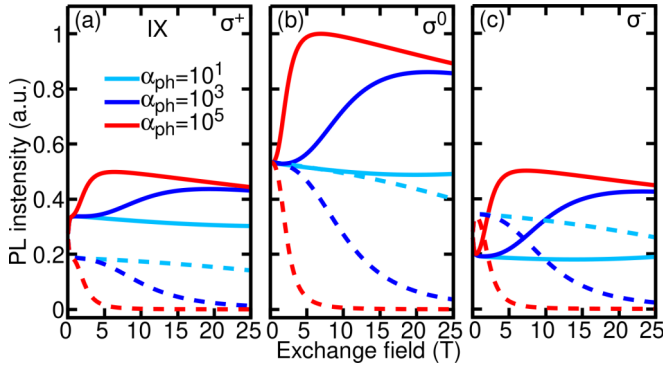


FIG. 11. PL intensity of IX emissions, excited by (a) σ^+ , (b) linear, and (c) σ^- lights, as a function of magnetic field at $\gamma_{13} = (70 \text{ ps})^{-1}$ and $T = 4.5 \text{ K}$, for different values of α_{ph} . Solid and dashed curves represent the PL intensities of IX emissions in α and β valleys, respectively. α_{ph} is in the unit of $\text{ps}^{-1}\text{eV}^{-3}$.

with the one in β valley, see the solid and dashed curves in Figs. 11(a) and 11(c). We also notice that in the presence of MPE (nonzero J_{ex}), the PL intensity of IX emission can be effectively tailored by a combination of exchange field, excitation light polarization and exciton-phonon coupling strength. In general, the exchange field promotes the IX emissions in α valley, whereas it weakens the IX emissions in β valley. The quantitative dependence of PL intensity on exchange field relies on the exciton-phonon coupling strength and excitation light polarization. For instance, for σ^+ excitation at $\alpha_{ph} = 10^5 \text{ ps}^{-1}\text{eV}^{-3}$, as the exchange field increases, the PL intensity of the IX in α valley grows up till its maximum. After that it starts to decrease slightly. In contrast, the PL intensity falls down monotonically in β valley, see Fig. 11(a). This is attributed to the interplay between the exchange field mediated radiative relaxation rate and intervalley scattering rate. With increasing the exchange field, the phonon mediated intervalley scattering rate from β to α valley is enlarged. For such a high value of α_{ph} , the exchange field mediated intervalley scattering is able to scatter all of the excitons in β valley into α valley. Hence, the σ^- PL intensity tends to vanishing small at $J_{ex} = 5 \text{ T}$, see the dashed lines. On the other side, the radiative relaxation process from state $|1\rangle$ to $|0\rangle$ is intensified. Then there are less number of the photon-created excitons in WS_2 layer being transferred to IXs. As a result, the intensity of IX emission in α valley reduces. Interestingly, for the system with a reduced α_{ph} such as $\alpha_{ph} = 10^3 \text{ ps}^{-1}\text{eV}^{-3}$, the variation rate of the PL intensity is much smaller than that of $\alpha_{ph} = 10^5 \text{ ps}^{-1}\text{eV}^{-3}$ due to weakness of intervalley scattering. For a even small α_{ph} , the PL intensity becomes insensitive to the variation of exchange field, see the PL intensity curves of $\alpha_{ph} = 10 \text{ ps}^{-1}\text{eV}^{-3}$. Furthermore, the PL intensity of IX emissions shows a strong dependence upon the excitation light polarization, see Figs. 11(a), 11(b), and 11(c). For instance, in the regime of small J_{ex} ($J_{ex} < 5 \text{ T}$), the PL intensity in α valley is stronger than β valley for both σ^+ and linearly polarized light excitations, while an opposite behavior is observed for σ^- light excitation.

Up to now, we mainly focus on the tunability of the IX emission intensity. Since the VP of IX emissions is dictated by the PL intensity, logically, we could speculate that the VP

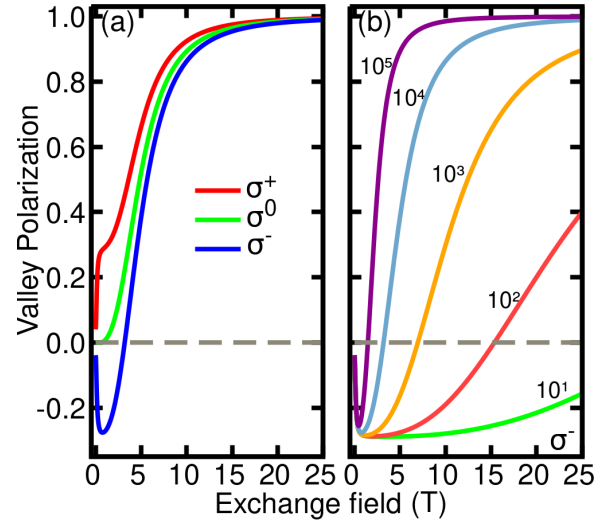


FIG. 12. Valley polarizations of IX emissions as a function of exchange field in MoS_2/WS_2 heterostructure grown on a magnetic substrate at $T = 4.5 \text{ K}$ and $\gamma_{13} = (70 \text{ ps})^{-1}$. (a) For different excitation laser helicity, at $\alpha_{ph} = 5 \times 10^3 \text{ ps}^{-1}\text{eV}^{-3}$. The blue and red curves correspond to circularly polarized σ^+ and σ^- laser excitations, while the black one is obtained by linearly polarized laser excitation. (b) For different α_{ph} . Green-dotted line separates positive and negative valley polarization, for eye guidance.

might also be controlled externally. Figure 12 shows the VP of IX emissions as a function of exchange field for different excitation laser polarization (a) and exciton-phonon coupling strength (α_{ph}) (b) at $T = 4.5 \text{ K}$ and $\gamma_{13} = (70 \text{ ps})^{-1}$. We notice that the excitation laser polarization, α_{ph} combined with exchange field J_{ex} are really a versatile tool, which can be used to tune the VP of the IX emissions. Figure 12(a) illustrates that in the regime of large J_{ex} such as $J_{ex} > 7 \text{ T}$, VP is higher than 0.8. For $J_{ex} \geq 10 \text{ T}$, all of three VPs, regardless of the excitation polarization, reach almost unity. This giant VP is attributed to an occupation imbalance between the Zeeman split IX states in two different valleys due to huge VS. Nevertheless, in the regime of small J_{ex} , the VP illustrates a strong excitation laser polarization dependence, especially for $J_{ex} \leq 5 \text{ T}$. In particular, at zero-exchange field, all of three curves exhibit very small VP due to strong electron-hole exchange Coulomb interaction. In more detail, in the absence of MPE, the IX emission hosts a positive (negative) VP for σ^+ (σ^-) excitation, while it exhibits a positive VP for linearly polarized light excitation. In addition, when J_{ex} increases from zero, the VP of IX emission stimulated by either σ^+ or linearly polarized light shows a monotonic enhancement. Nevertheless, the VP of the IX emission excited by σ^- laser displays a nonmonotonic behavior. With an increase of J_{ex} , the negative VP initially increases due to a suppression of the depolarization induced by electron-hole exchange interaction. Although the phonon mediated intervalley scattering tends to reduce the negative VP, its intervalley scattering rate is smaller than that of electron-hole exchange interaction, see the curves of total scattering rate in Fig. 6. With a further increase of the exchange field, the former becomes bigger than the latter. Then the negative VP starts to decrease. At $J_{ex} = 4.1 \text{ T}$, the VP turns to be zero. After that, the VP

switches its sign and monotonically increases with raising exchange field. At moderate value of J_{ex} (about 20 T), all of three VP curves reaches 1. Remarkably, the exchange field dependence of the VP can be dramatically tuned by exciton-phonon coupling strength, see Fig. 12(b). For a large value of α_{ph} , the depolarization induced by the electron-hole exchange interaction is quickly suppressed by the exchange field and the VP reaches its maximum value at a small value of J_{ex} (~ 6 T). With a reduction of α_{ph} , the phonon-assisted intervalley scattering is slowed down. Then a larger exchange field is required to overcome this VP depolarization. In addition, the slope of exchange field enhancement of the VP becomes smaller. As a result, a saturation of the VP is reached only at higher exchange field. For the heterostructure with a very weak exciton-phonon coupling such as $\alpha_{ph} = 10 \text{ ps}^{-1}\text{eV}^{-3}$, the phonon-assisted intervalley transition is too weak to drive the VP switching its sign, see the curve marked by 10. Therefore, the combination of α_{ph} and J_{ex} can be used as an efficient tool to manipulate magneto-optics, and to precisely control the VP from 0 to almost 100%. It is worth pointing out that the value of α_{ph} can be changed by use of gating or variation of interlayer distance, while the J_{ex} can be altered by changing ferromagnetic substrate or applying a small magnetic field. Therefore, the tunability of both PL intensity and VP of IX emission are accessible experimentally.

IV. CONCLUSIONS

In this paper, we studied the valley dynamics of interlayer excitons (IXs) in MoS_2/WS_2 heterostructure with AB stacking configuration grown on ferromagnetic substrate, utilizing theoretical tools such as first principles calculation, $\mathbf{k} \cdot \mathbf{p}$ approach including excitons and coupled rate equations. Our main findings reveal that the interlayer charge transfer process changes dramatically the interlayer exciton (IX) emission as well as its VP. The ratio of I_3 and I_1 can be amplified as high as four orders of magnitude when τ_{13} is shortened from 70 to 0.07 ps. The MPE exerted by ferromagnetic substrate, on the other hand, generates a zero-field valley Zeeman splitting, leading to a suppression of the depolarization induced by electron-hole exchange interaction. Furthermore, as exchange field raises, the VP of IX emission in β valley switches its sign from negative to positive one. Remarkably, unlike usual exciton-phonon scattering, which is harmful to the VP, the phonon-assisted intervalley scatterings between two split IX states in the different valleys promote an IX population imbalance in these states, giving rise to a giant VP. Therefore, a combination of these experimentally tunable physical quantities (interlayer charge transfer rate, MPE intensity and exciton-phonon coupling strength) provides a valuable tool for intriguing emerging magneto-optical emissions and their VPs. Because the radiation and the valley lifetimes of the IXs are substantially prolonged in comparison with those observed in TMD monolayers, together with the ease with which the optical properties of the heterostructures can be largely tuned, our results pave the way for controlling the properties of IXs as well as for the development of van der Waals heterostructures with detectable IX emissions and giant VP.

TABLE II. Optimized parameters for the full optimization. All parameters are in eV.

	$\text{MoS}_2 (i=1)$	$\text{WS}_2 (i=2)$
E_F	-1.7068	-0.8690
Δ	1.6513	1.7478
λ_c	0.0030	-0.0069
λ_v	0.0740	0.1890
$\delta_{0,i}$	0.9935	1.2001
$\delta_{1,i}$	0.0020	0.1495
$\delta_{2,i}$	0.0401	0.0985
$\delta_{3,i}$	0.1562	0.3042
$\delta_{4,i}$	-0.0208	-0.2934
$\delta_{5,i}$	-0.0396	0.0718
$\delta_{6,i}$	-0.2010	-0.3018
a	3.16 Å	3.17 Å

ACKNOWLEDGMENTS

This work was supported by CNPq, FAPDF, and Coordenação de Aperfeiçoamento de Pessoal de Nível Superior - Brasil (CAPES) - Finance Code 001. F.R. acknowledge support by FCT through Grant No. UIDB/04540/2020. We are grateful to J. H. Correa and Vilmara Vilmara Paixão for valuable discussions.

APPENDIX A: SIMULATED ANNEALING FITTING FOR DFM PARAMETER ESTIMATION

The parameters used to construct DFM Hamiltonian can be obtained by fitting the band structure obtained by the model to that of first principles calculation. To do so, we perform the simulated annealing (SA), which is a general designation for a class of methods for nonlinear optimization, which employ a stochastic approach to find the global minimum of a given function in a large search space. In SA, Monte Carlo (MC) method is adopted in which the equilibrium of a system with many coupled degrees of freedom is simulated by sampling the most significative states of its phase space, whose corresponding energies are characterized by the set of parameters $\{F_i\}$, $i = 1, \dots, N_p$. Starting from an initial guess of the set $\{F_i\}$, new sets are generated following a Markov chain, with the acceptance of new values governed by the Metropolis algorithm. In order to implement the algorithm, a merit function of the parameters set $\Gamma(\{F_i\})$ should be supplied. For typical applications of the Monte Carlo method, the energy $\Gamma = E(\{F_i\})$ of the system has been chosen as the merit function. The changes of the parameters that decrease the system's merit function are

TABLE III. Optimized parameters considering only the linear expansion of DFM Hamiltonian. All parameters are in eV.

	$\text{MoS}_2 (i=1)$	$\text{WS}_2 (i=2)$
E_F	-1.7059	-0.8491
Δ	1.6505	1.7470
λ_c	0.0030	-0.0069
λ_v	0.0740	0.1890
$\delta_{0,i}$	0.8646	0.9827
a	3.16 Å	3.17 Å

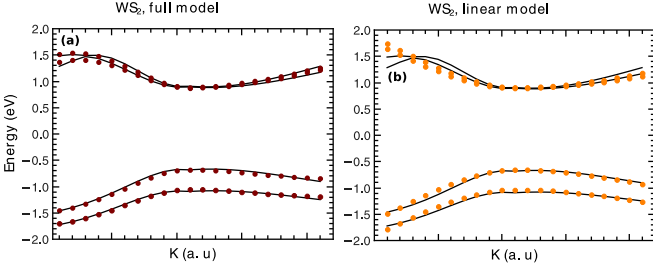


FIG. 13. Comparison among the DFT (lines) and the $\mathbf{k} \cdot \mathbf{p}$ (dots) bands for WS_2 .

always accepted, whereas those, which increase are accepted within given probability, proportional to the Boltzmann factor $e^{-\frac{\Delta\Gamma}{k_B T}}$, where T is the temperature (a fictitious temperature) and k_B the Boltzmann constant. The role of the temperature is controlling the acceptance of the new parameter's set, which raise the system energy, resulting in $\Delta\Gamma > 0$: for high values of $k_B T$ compared to $\Delta\Gamma$ all changes on the parameter's values are accepted. On the other hand, if $k_B T$ is small in comparison with $\Delta\Gamma$, the generated new set is always rejected. According this procedure, the system evolves from an artificial initial state, related to the initial guess of $(\{F_i\})$, to equilibrium states whose corresponding energy values have a well defined average \bar{E} . The instantaneous energy values E_i , corresponding to the energies of all accepted sets of parameters, fluctuate around \bar{E} with amplitude proportional to the system temperature T . As mentioned before, the Monte Carlo method is employed to seek the optimal parameter set for a given Hamiltonian model, successive Monte Carlo cycles with decreasing temperatures are performed, allowing to find the global minimum of the problem. Along a SA simulation, the variance of the parameter values decrease systematically due the temperature reduction until the parameters freeze at the values corresponding to the minimum energy. In the present application of the SA method, the adopted merit (objective) function is the root mean square, which account the deviation of the theoretical values of the $\mathbf{k} \cdot \mathbf{p}$ bands from the respective target values, here taken from DFT calculations,

$$\Gamma(\{F_i\}) = \sqrt{\frac{\sum_{n=1}^N \sum_{m=1}^M [E_{n,m}^{Th} - E_{n,m}^{DFT}]^2}{NM}}, \quad (\text{A1})$$

where n runs over the bands, m over the k points along the chosen path, and the index i in the equation (A1) labels the set of parameters of the DFM Hamiltonian. Moreover, Th

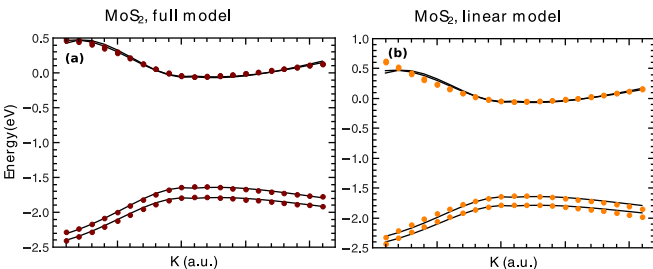


FIG. 14. Comparison among the DFT (lines) and the $\mathbf{k} \cdot \mathbf{p}$ (dots) bands for MoS_2 .

TABLE IV. Parameters involving in DFM for the WS_2/MoS_2 van der Waals heterostructure.

ϵ_c^1 (eV)	2.3090
ϵ_v^1 (eV)	0.4189
ϵ_c^2 (eV)	2.5870
ϵ_v^2 (eV)	0.9557
a (Å)	3.18
t (eV/Å ²)	0.06

and DFT in (A1) denote, respectively, the theoretical (DFM) and the target energy values, here the DFT band structure. The SA approach adopted in this article correspond to the Vanderbilt [55] proposal, suitable for problems where the parameters of the objective function are continuous variables. In the minimization procedure, all nonzero transitions were included in equation (A1) and an acceptable set was generated when $\Gamma < 0.1$ eV. The present SA proposal was successfully applied in the determination of the Hamiltonian parameters of a extended Hückel Hamiltonian for crystalline semiconductors [56,57].

1. Parameter fitting for the MoS_2 and WS_2 monolayers

We have performed two types of fittings: full optimization fitting and a linear model fitting. In the former, all parameters are allowed to vary, while all δ parameters are set to zero, except δ_0 in the latter. Moreover, for the linear model we constraint the spin-orbit parameters to the values determined in the full optimization. The Tables II and III summarize the calculated optimized parameters.

A comparison between the DFT target bands and DFM predicted ones for both full and linear models are presented in Figs. 13 and 14. We can notice that the overall agreement is very good.

APPENDIX B: LIFETIME OF DX AND IXS IN TMD VDWS HETEROSTRUCTURES

Let us evaluate the lifetimes of the DX and IX in MoS_2/WS_2 heterostructure. For simplicity, we adopt the low-energy model for single-particle calculations, as presented in the main text. In addition, considering the interlayer coupling between the CBs of two layers is weaker than that of VBs and the higher-order terms of q in Hamiltonian do not make a significant contribution, we only take into account the interlayer couplings between the VBs of two layers [$t_h = t$ and $t_e = 0$, see Eq. (11)] and the linear term in q [H_0^i in Eq. (1)]. Based on these considerations, the matrix of the Hamiltonian $\hat{H}_{sp}(\mathbf{q})$ for spin-up (\uparrow) states in the basis of

TABLE V. Exciton binding energies [58].

$\epsilon_{b,1}$ (eV)	0.60
$\epsilon_{b,2}$ (eV)	0.57
$\epsilon_{b,IX}$ (eV)	0.51

TABLE VI. Calculated radiative lifetimes of DX and IX in the WS₂/MoS₂ vdWs heterostructure. $\tau_{0,0K}$ and $\tau_{0,4.5K}$ refer to the lifetimes of corresponding excitons at T = 0 and 4.5 K, respectively.

	E_{ex}^s/eV	m_e/m_h	$\tau_{0,0K}/ps$	$\langle\tau_{0,4.5K}\rangle/ps$
DX	1.057	0.37/0.32	0.003	4.27
IX _S	0.838	0.64/0.32	0.65	1634

$\{|c^1, \uparrow\rangle, |v^1, \uparrow\rangle, |c^2, \uparrow\rangle, |v^2, \uparrow\rangle\}$, can be written as

$$\hat{H}_{sp}(\mathbf{q}) = \begin{pmatrix} \epsilon_c^1 & q_-^1 & 0 & 0 \\ q_+^1 & \epsilon_v^1 & 0 & t \\ 0 & 0 & \epsilon_c^2 & q_-^2 \\ 0 & t & q_+^2 & \epsilon_v^2 \end{pmatrix}, \quad (B1)$$

where $L = \{1, 2\}$ is layer index (1 \rightarrow MoS₂, 2 \rightarrow WS₂), ϵ_n^L and $|n^L, \uparrow\rangle$ are the energy and wavefunction of the n th band

$$\hat{H}_{exc} = \begin{pmatrix} \epsilon_c^1 - \epsilon_v^1 - \epsilon_{b,1} & t & 0 & 0 \\ t & \epsilon_c^1 - \epsilon_v^2 - \epsilon_{b,IX} & 0 & 0 \\ 0 & 0 & \epsilon_c^2 - \epsilon_v^1 - \epsilon_{b,IX} & t \\ 0 & 0 & t & \epsilon_c^2 - \epsilon_v^2 - \epsilon_{b,2} \end{pmatrix}, \quad (B2)$$

where t is the interlayer coupling of Eq. (B1) and the parameters $\epsilon_{b,1}$, $\epsilon_{b,2}$, and $\epsilon_{b,IX}$ are the exciton binding energies shown in Table V.

Solving Eq. (B2), we obtain the exciton wavefunctions, $|\Psi_s\rangle = \sum_{c,v,\mathbf{k}} A_{c,v,\mathbf{k}}^s |c, \mathbf{k}; v, \mathbf{k}\rangle$, from which we can calculate exciton lifetimes as following. We study the recombinations of the excitons located within the light cone nearby the K point. At $T = 0$ K, the radiative lifetime of an exciton is determined by

$$\tau_S^{-1}(0) = \frac{8\pi\alpha E_{ex}^s \mu_S^2}{A_{uc} \hbar}, \quad (B3)$$

where $\alpha = \frac{e^2}{4\pi\epsilon_0\hbar c} = 137^{-1}$, A_{uc} is the unit-cell area and μ_S is dipole moment. At finite temperature, the corresponding exciton lifetime is governed by

$$\langle\tau_S\rangle = \tau_S(0) \frac{3}{4} \left(\frac{E_{ex}^s}{2Mc^2} \right)^{-1} k_B T, \quad (B4)$$

where M is effective mass of the exciton, defined by $M = (m_e + m_h)m_0$ with m_e and m_h representing the effective mass of electron and hole, respectively, m_0 being free-electron mass, k_B is the Boltzmann constant, and T is the temperature. The term of μ_S is given by

$$\mu_S = \frac{\hbar}{m_0 E_{ex}^s} |\langle G | p_{||} | \Psi_s \rangle| = \frac{1}{N_q E_{ex}^s} \sum_{c,v,\mathbf{q}} A_{c,v,\mathbf{q}}^s \left\langle c, \mathbf{q} \left| \frac{\partial H_{sp}}{\partial q_{||}} \right| v, \mathbf{q} \right\rangle, \quad (B5)$$

where N_q is the number of \mathbf{q} vectors around K (K') points, $p_{||}$ is the momentum operator in an arbitrary in-plane direction, which was chosen along the x axis. We evaluate the

($n = c/v$) spin-up electronic state in the individual L layer. c (v) denotes CB and VB, $q_{\pm}^L = at^L(\tau q_x \pm iq_y)$ with a and t^L being the lattice parameter and the hopping energy in L layer. The parameters listed in Table IV are obtained by fitting the low-energy model output with DFT results for the WS₂/MoS₂ vdWs heterostructure. They are in accordance with reference [58]. The eigenvalues and eigenstates ($|c, \mathbf{q}\rangle$, $|v, \mathbf{q}\rangle$) of single-particle in WS₂/MoS₂ heterostructure can be obtained by diagonalizing the matrix of $\hat{H}_{sp}(\mathbf{q})$.

Now let us move our attention to the calculation of the energy bands of excitons around K and K' points. The matrix Hamiltonian of the low-energy excitons with a given spin in MoS₂/WS₂ heterostructure, considering a basis composed by the product of electron and hole wave functions, $\{|c^1 v^1\rangle, |c^1 v^2\rangle, |c^2 v^1\rangle, |c^2 v^2\rangle\}$ (with the wave number \mathbf{k} absorbed in the band index c and v : $|c^i v^j\rangle = |c^i, \mathbf{k}\rangle \otimes |v^j, \mathbf{k}\rangle$); we consider only excitons with zero center of mass momentum), is given by

lifetimes of the excitons including IX_S (the state comprised mainly by c^2 and v^2 , although the interlayer coupling t leads to a small band mixture) and DX (comprised mainly by c^1 and v^2) at zero and finite temperatures, using Eqs. (B3) and (B4) combining with (B5), and list the results in Table VI.

APPENDIX C: PARAMETERS USED IN THE CALCULATION OF IX DYNAMICS

Table VII summarizes the parameters used in the exciton dynamics throughout this work, as described in the main text.

TABLE VII. Parameters used in exciton dynamics for MoS₂/WS₂ van der Waals heterostructure.

Scattering rate	Value
$\gamma_{10}(ps^{-1})$	$(2.85e^{(-B/6.29T)} + 1.42)^{-1}$
$\gamma_{30}(ps^{-1})$	$(1089e^{(-B/6.29T)} + 545)^{-1}$
$\gamma_{13}(ps^{-1})$	$\frac{1}{70}$
P_0	-0.29
$\gamma_{13'}(ps^{-1})$	$\gamma_{13} \frac{1-P_0}{1+P_0}$
$\gamma_{11'}(ps^{-1})$	$\frac{1}{20.10^3} \frac{(4.10^{-5})^2}{(4.10^{-5})^2 + (\Delta E_{11'})^2} + \frac{1.10^4 \Delta E_{11'} ^3}{ e^{\Delta E_{11'}/k_B T} - 1 }$
$\gamma_{1'1}(ps^{-1})$	$\frac{1}{20.10^3} \frac{(4.10^{-5})^2}{(4.10^{-5})^2 + (\Delta E_{1'1})^2} + \frac{1.10^4 \Delta E_{1'1} ^3}{ e^{-\Delta E_{1'1}/k_B T} - 1 }$
$\gamma_{33'}(ps^{-1})$	$\frac{1}{20.10^3} \frac{(4.10^{-5})^2}{(4.10^{-5})^2 + (\Delta E_{33'})^2} + \frac{1.10^4 \Delta E_{33'} ^3}{ e^{\Delta E_{33'}/k_B T} - 1 }$
$\gamma_{3'3}(ps^{-1})$	$\frac{1}{20.10^3} \frac{(4.10^{-5})^2}{(4.10^{-5})^2 + (\Delta E_{3'3})^2} + \frac{1.10^4 \Delta E_{3'3} ^3}{ e^{-\Delta E_{3'3}/k_B T} - 1 }$

- [1] S. Mouri, Y. Miyauchi, M. Toh, W. Zhao, G. Eda, and K. Matsuda, Nonlinear photoluminescence in atomically thin layered WSe₂ arising from diffusion-assisted exciton-exciton annihilation, *Phys. Rev. B* **90**, 155449 (2014).
- [2] A. C. Dias, J. Fu, L. Villegas-Lelovsky, and F. Qu, Robust effective Zeeman energy in monolayer MoS₂ quantum dots, *J. Phys.: Condens. Matter* **28**, 375803 (2016).
- [3] F. Riche, H. Bragança, F. Qu, V. Lopez-Richard, S. J. Xie, A. C. Dias, and G. E. Marques, Robust room temperature emissions of trion in darkish WSe₂ monolayers: Effects of dark neutral and charged excitonic states, *J. Phys.: Condens. Matter* **32**, 365702 (2020).
- [4] T. Godde, D. Schmidt, J. Schmutzler, M. Aßmann, J. Debus, F. Withers, E. M. Alexeev, O. D. Pozo-Zamudio, O. V. Skrypka, K. S. Novoselov, M. Bayer, and A. I. Tartakovskii, Exciton and trion dynamics in atomically thin MoSe₂ and WSe₂: Effect of localization, *Phys. Rev. B* **94**, 165301 (2016).
- [5] C. Robert, D. Lagarde, F. Cadiz, G. Wang, B. Lassagne, T. Amand, A. Balocchi, P. Renucci, S. Tongay, B. Urbaszek, and X. Marie, Exciton radiative lifetime in transition metal dichalcogenide monolayers, *Phys. Rev. B* **93**, 205423 (2016).
- [6] K. F. Mak, K. He, C. Lee, G. H. Lee, J. Hone, T. F. Heinz, and J. Shan, Tightly bound trions in monolayer MoS₂, *Nat. Mater.* **12**, 207 (2012).
- [7] A. Ciarrocchi, F. Tagarelli, A. Avsar, and A. Kis, Excitonic devices with van der Waals heterostructures: Valleytronics meets twistrionics, *Nat. Rev. Mater.* **7**, 449 (2022).
- [8] Y. Li, J. Ludwig, T. Low, A. Chernikov, X. Cui, G. Arefe, Y. D. Kim, A. M. van der Zande, A. Rigosi, H. M. Hill, S. H. Kim, J. Hone, Z. Li, D. Smirnov, and T. F. Heinz, Valley Splitting and Polarization by the Zeeman Effect in Monolayer MoSe₂, *Phys. Rev. Lett.* **113**, 266804 (2014).
- [9] A. A. Mitioglu, P. Plochocka, Á. G. del Aguila, P. C. M. Christianen, G. Deligeorgis, S. Anghel, L. Kulyuk, and D. K. Maude, Optical investigation of monolayer and bulk tungsten diselenide (WSe₂) in high magnetic fields, *Nano Lett.* **15**, 4387 (2015).
- [10] Y. Zhao, L. Du, S. Yang, J. Tian, X. Li, C. Shen, J. Tang, Y. Chu, K. Watanabe, T. Taniguchi, R. Yang, D. Shi, Z. Sun, Y. Ye, W. Yang, and G. Zhang, Interlayer exciton complexes in bilayer MoS₂, *Phys. Rev. B* **105**, L041411 (2022).
- [11] D. Huang, J. Choi, C.-K. Shih, and X. Li, Excitons in semiconductor moiré superlattices, *Nat. Nanotechnol.* **17**, 227 (2022).
- [12] Z. Li, X. Lu, D. F. C. Leon, Z. Lyu, H. Xie, J. Hou, Y. Lu, X. Guo, A. Kaczmarek, T. Taniguchi, K. Watanabe, L. Zhao, L. Yang, and P. B. Deotare, Interlayer exciton transport in MoSe₂/WSe₂ heterostructures, *ACS Nano* **15**, 1539 (2021).
- [13] M. Förg, A. S. Baimuratov, S. Y. Kruchinin, I. A. Vovk, J. Scherzer, J. Förste, V. Funk, K. Watanabe, T. Taniguchi, and A. Högele, Moiré excitons in MoSe₂-WSe₂ heterobilayers and heterotrilayers, *Nat. Commun.* **12**, 1656 (2021).
- [14] K. Tran, G. Moody, F. Wu, X. Lu, J. Choi, K. Kim, A. Rai, D. A. Sanchez, J. Quan, A. Singh *et al.*, Evidence for moiré excitons in van der Waals heterostructures, *Nature (London)* **567**, 71 (2019).
- [15] E. M. Alexeev, D. A. Ruiz-Tijerina, M. Danovich, M. J. Hamer, D. J. Terry, P. K. Nayak, S. Ahn, S. Pak, J. Lee, J. I. Sohn *et al.*, Resonantly hybridized excitons in moiré superlattices in van der Waals heterostructures, *Nature (London)* **567**, 81 (2019).
- [16] K. L. Seyler, P. Rivera, H. Yu, N. P. Wilson, E. L. Ray, D. G. Mandrus, J. Yan, W. Yao, and X. Xu, Signatures of moiré-trapped valley excitons in MoSe₂/WSe₂ heterobilayers, *Nature (London)* **567**, 66 (2019).
- [17] P. Rivera, H. Yu, K. L. Seyler, N. P. Wilson, W. Yao, and X. Xu, Interlayer valley excitons in heterobilayers of transition metal dichalcogenides, *Nat. Nanotechnol.* **13**, 1004 (2018).
- [18] L. Zhang, R. Gogna, G. W. Burg, J. Horng, E. Paik, Y.-H. Chou, K. Kim, E. Tutuc, and H. Deng, Highly valley-polarized singlet and triplet interlayer excitons in van der Waals heterostructure, *Phys. Rev. B* **100**, 041402 (2019).
- [19] E. Barré, O. Karni, E. Liu, A. L. O’Beirne, X. Chen, H. B. Ribeiro, L. Yu, B. Kim, K. Watanabe, T. Taniguchi *et al.*, Optical absorption of interlayer excitons in transition-metal dichalcogenide heterostructures, *Science* **376**, 406 (2022).
- [20] Y. Liu, A. Elbanna, W. Gao, J. Pan, Z. Shen, and J. Teng, Interlayer excitons in transition metal dichalcogenide semiconductors for 2D optoelectronics, *Adv. Mater.* **34**, 2107138 (2022).
- [21] J. Qi, X. Li, Q. Niu, and J. Feng, Giant and tunable valley degeneracy splitting in MoTe₂, *Phys. Rev. B* **92**, 121403(R) (2015).
- [22] Q. Zhang, S. A. Yang, W. Mi, Y. Cheng, and U. Schwingenschlögl, Large spin-valley polarization in monolayer MoTe₂ on top of EuO(111), *Adv. Mater.* **28**, 959 (2015).
- [23] T. Norden, C. Zhao, P. Zhang, R. Sabirianov, A. Petrou, and H. Zeng, Giant valley splitting in monolayer WS₂ by magnetic proximity effect, *Nat. Commun.* **10**, 4163 (2019).
- [24] A. V. Stier, K. M. McCreary, B. T. Jonker, J. Kono, and S. A. Crooker, Exciton diamagnetic shifts and valley zeeman effects in monolayer WS₂ and MoS₂ to 65 Tesla, *Nat. Commun.* **7**, 10643 (2016).
- [25] A. C. Dias, H. Bragança, H. Zeng, A. L. A. Fonseca, D.-S. Liu, and F. Qu, Large room-temperature valley polarization by valley-selective switching of exciton ground state, *Phys. Rev. B* **101**, 085406 (2020).
- [26] H. Bragança, H. Zeng, A. C. Dias, J. H. Correa, and F. Qu, Magnetic-gateable valley exciton emission, *npj Comput. Mater.* **6**, 90 (2020).
- [27] P. Nagler, M. V. Ballottin, A. A. Mitioglu, F. Mooshammer, N. Paradiso, C. Strunk, R. Huber, A. Chernikov, P. C. M. Christianen, C. Schüller, and T. Korn, Giant magnetic splitting inducing near-unity valley polarization in van der Waals heterostructures, *Nat. Commun.* **8**, 1551 (2017).
- [28] T. Wang, S. Miao, Z. Li, Y. Meng, Z. Lu, Z. Lian, M. Blei, T. Taniguchi, K. Watanabe, S. Tongay *et al.*, Giant valley-zeeman splitting from spin-singlet and spin-triplet interlayer excitons in WSe₂/MoSe₂ heterostructure, *Nano Lett.* **20**, 694 (2019).
- [29] A. Surrente, Ł. Kłopotowski, N. Zhang, M. Baranowski, A. A. Mitioglu, M. V. Ballottin, P. C. Christianen, D. Dumcenco, Y.-C. Kung, D. K. Maude, A. Kis, and P. Plochocka, Intervalley scattering of interlayer excitons in a MoS₂/MoSe₂/MoS₂ heterostructure in high magnetic field, *Nano Lett.* **18**, 3994 (2018).
- [30] G. Kresse and J. Hafner, *Ab initio* molecular dynamics for open-shell transition metals, *Phys. Rev. B* **48**, 13115 (1993).

- [31] G. Kresse and J. Furthmüller, Efficient iterative schemes for *ab initio* total-energy calculations using a plane-wave basis set, *Phys. Rev. B* **54**, 11169 (1996).
- [32] J. P. Perdew, K. Burke, and M. Ernzerhof, Generalized Gradient Approximation Made Simple, *Phys. Rev. Lett.* **77**, 3865 (1996).
- [33] S. Grimme, J. Antony, S. Ehrlich, and H. Krieg, A consistent and accurate *ab initio* parametrization of density functional dispersion correction (DFT-D) for the 94 elements H-Pu, *J. Chem. Phys.* **132**, 154104 (2010).
- [34] E. Torun, H. P. C. Miranda, A. Molina-Sánchez, and L. Wirtz, Interlayer and intralayer excitons in MoS₂/WS₂ and MoSe₂/WSe₂ heterobilayers, *Phys. Rev. B* **97**, 245427 (2018).
- [35] H.-P. Komsa and A. V. Krasheninnikov, Electronic structures and optical properties of realistic transition metal dichalcogenide heterostructures from first principles, *Phys. Rev. B* **88**, 085318 (2013).
- [36] Y. Yu, S. Hu, L. Su, L. Huang, Y. Liu, Z. Jin, A. A. Purezky, D. B. Geohegan, K. W. Kim, Y. Zhang, and L. Cao, Equally efficient interlayer exciton relaxation and improved absorption in epitaxial and nonepitaxial MoS₂/WS₂ heterostructures, *Nano Lett.* **15**, 486 (2014).
- [37] C. S. Tang, X. Yin, M. Yang, D. Wu, M. D. Birowosuto, J. Wu, C. Li, C. Hettiarachchi, X. Y. Chin, Y.-H. Chang *et al.*, Three-dimensional resonant exciton in monolayer tungsten diselenide actuated by spin-orbit coupling, *ACS Nano* **13**, 14529 (2019).
- [38] J. F. R. V. Silveira, R. Besse, A. C. Dias, N. A. M. S. Caturello, and J. L. F. D. Silva, Tailoring excitonic and optoelectronic properties of transition metal dichalcogenide bilayers, *J. Phys. Chem. C* **126**, 9173 (2022).
- [39] D. Xiao, M.-C. Chang, and Q. Niu, Berry phase effects on electronic properties, *Rev. Mod. Phys.* **82**, 1959 (2010).
- [40] F. Zhang, J. Jung, G. A. Fiete, Q. Niu, and A. H. MacDonald, Spontaneous Quantum Hall States in Chirally Stacked Few-Layer Graphene Systems, *Phys. Rev. Lett.* **106**, 156801 (2011).
- [41] A. Kormányos, V. Zólyomi, V. I. Fal'ko, and G. Burkard, Tunable berry curvature and valley and spin hall effect in bilayer MoS₂, *Phys. Rev. B* **98**, 035408 (2018).
- [42] M.-C. Chang and Q. Niu, Berry phase, hyperorbits, and the Hofstadter spectrum: Semiclassical dynamics in magnetic Bloch bands, *Phys. Rev. B* **53**, 7010 (1996).
- [43] T. Cai, S. A. Yang, X. Li, F. Zhang, J. Shi, W. Yao, and Q. Niu, Magnetic control of the valley degree of freedom of massive Dirac fermions with application to transition metal dichalcogenides, *Phys. Rev. B* **88**, 115140 (2013).
- [44] T. Fukui, Y. Hatsugai, and H. Suzuki, Chern numbers in discretized Brillouin zone: Efficient method of computing (spin) Hall conductances, *J. Phys. Soc. Jpn.* **74**, 1674 (2005).
- [45] D. S. Brandão, E. C. Castro, H. Zeng, J. Zhao, G. S. Diniz, J. Fu, A. L. A. Fonseca, C. A. N. Júnior, and F. Qu, Phonon-fostered valley polarization of interlayer excitons in van der Waals heterostructures, *J. Phys. Chem. C* **126**, 18128 (2022).
- [46] F. Wu, F. Qu, and A. H. MacDonald, Exciton band structure of monolayer MoS₂, *Phys. Rev. B* **91**, 075310 (2015).
- [47] P.-Y. Lo, G.-H. Peng, W.-H. Li, Y. Yang, and S.-J. Cheng, Full-zone valley polarization landscape of finite-momentum exciton in transition metal dichalcogenide monolayers, *Phys. Rev. Res.* **3**, 043198 (2021).
- [48] M. Okada, A. Kutana, Y. Kureishi, Y. Kobayashi, Y. Saito, T. Saito, K. Watanabe, T. Taniguchi, S. Gupta, Y. Miyata, B. I. Yakobson, H. Shinohara, and R. Kitaura, Direct and indirect interlayer excitons in a van der Waals heterostructure of hBN/WS₂/MoS₂/hBN, *ACS Nano* **12**, 2498 (2018).
- [49] T. Yu and M. W. Wu, Valley depolarization due to intervalley and intravalley electron-hole exchange interactions in monolayer MoS₂, *Phys. Rev. B* **89**, 205303 (2014).
- [50] M. Selig, F. Katsch, R. Schmidt, S. Michaelis de Vasconcellos, R. Bratschitsch, E. Malic, and A. Knorr, Ultrafast dynamics in monolayer transition metal dichalcogenides: Interplay of dark excitons, phonons, and intervalley exchange, *Phys. Rev. Res.* **1**, 022007(R) (2019).
- [51] A. Raja, M. Selig, G. Berghäuser, J. Yu, H. M. Hill, A. F. Rigosi, L. E. Brus, A. Knorr, T. F. Heinz, E. Malic, and A. Chernikov, Enhancement of exciton-phonon scattering from monolayer to bilayer WS₂, *Nano Lett.* **18**, 6135 (2018).
- [52] X. Hong, J. Kim, S.-F. Shi, Y. Zhang, C. Jin, Y. Sun, S. Tongay, J. Wu, Y. Zhang, and F. Wang, Ultrafast charge transfer in atomically thin MoS₂/WS₂ heterostructures, *Nat. Nanotechnol.* **9**, 682 (2014).
- [53] Z. Wang, P. Altmann, C. Gadermaier, Y. Yang, W. Li, L. Ghirardini, C. Trovatiello, M. Finazzi, L. Duò, M. Celebrano *et al.*, Phonon-mediated interlayer charge separation and recombination in a MoSe₂/WSe₂ heterostructure, *Nano Lett.* **21**, 2165 (2021).
- [54] J. E. Zimmermann, M. Axt, F. Mooshammer, P. Nagler, C. Schüller, T. Korn, U. Höfer, and G. Mette, Ultrafast charge-transfer dynamics in twisted MoS₂/WSe₂ heterostructures, *ACS Nano* **15**, 14725 (2021).
- [55] D. Vanderbilt and S. G. Louie, A Monte Carlo simulated annealing approach to optimization over continuous variables, *J. Comput. Phys.* **56**, 259 (1984).
- [56] I. A. Ribeiro, F. J. Ribeiro, and A. Martins, An extended Hückel study of the electronic properties of III-V compounds and their alloys, *Solid State Commun.* **186**, 50 (2014).
- [57] A. de Souza Martins and M. Veríssimo-Alves, Group-IV nanosheets with vacancies: A tight-binding extended Hückel study, *J. Phys.: Condens. Matter* **26**, 365501 (2014).
- [58] S. Gao, L. Yang, and C. D. Spataru, Interlayer coupling and gate-tunable excitons in transition metal dichalcogenide heterostructures, *Nano Lett.* **17**, 7809 (2017).